JGR Atmospheres

RESEARCH ARTICLE
10.1029/2025JD044604

Modeling the Impact of Alternative Fuels and Hydrogen Propulsion on Contrail-Cirrus: A Parameter Study

Annemarie Lottermoser[1] and **Simon Unterstrasser**[1]

[1]Deutsches Zentrum für Luft- und Raumfahrt, Institut für Physik der Atmosphäre, Oberpfaffenhofen, Germany

Key Points:

- Ice crystal loss in hydrogen contrail-cirrus with low/high number of initial ice crystals is dominated by sedimentation/in situ sublimation
- Contrail-cirrus with low initial ice crystal numbers dissipate rapidly, potentially reducing their radiative impact
- The relationship between normalized total extinction and normalized initial ice crystal number is highly nonlinear

Correspondence to:
A. Lottermoser,
annemarie.lottermoser@dlr.de

Citation:
Lottermoser, A., & Unterstrasser, S. (2026). Modeling the impact of alternative fuels and hydrogen propulsion on contrail-cirrus: A parameter study. *Journal of Geophysical Research: Atmospheres*, *131*, e2025JD044604. https://doi.org/10.1029/2025JD044604

Received 13 JUN 2025
Accepted 24 DEC 2025

Abstract Line-shaped contrails formed behind aircraft can evolve into broadly spread and long-living cirrus clouds under favorable conditions. These contrail-cirrus contribute significantly to the aviation-induced radiative forcing. While past modeling studies have examined contrail-cirrus across various atmospheric and aircraft-type dependent parameters, they have focused on conventional kerosene combustion. In this study, we investigate how the switch to an alternative propulsion system, such as hydrogen combustion, may alter contrail-cirrus properties using the large-eddy simulation (LES) model EULAG coupled with the Lagrangian Cloud Module (LCM), a particle-based microphysics module. Building on prior work that modeled hydrogen contrails during the vortex phase, we use those results to initialize the subsequent contrail-cirrus evolution. We explore a wide range of background meteorological conditions, including variations of ambient temperature, relative humidity with respect to ice, vertical wind shear, and updraft velocity, and assess two aircraft types. Key contrail properties, such as total ice crystal number and mass, are found to be most sensitive to the initial number of ice crystals and ambient temperature. We show that reducing the number of initially formed ice crystals substantially decreases contrail radiative impact. This is primarily due to a shorter contrail-cirrus lifetime, driven by the earlier onset and more efficient sedimentation of the fewer but larger ice crystals. Moreover, the relationship between radiative impact and initial ice crystal number is nonlinear, consistent with previous studies.

Plain Language Summary When aircraft fly through cold and humid air, they can produce contrails that may evolve into cirrus clouds, so called contrail-cirrus. These contrail-cirrus can persist and spread, contributing to the climate impact of aviation. While many studies have modeled their behavior, they have mainly considered contrail-cirrus formed behind aircraft with conventional kerosene engines. This study examines how the switch to future aircraft powered by alternative fuels could change the characteristics of contrail-cirrus. Using earlier simulations of hydrogen contrails during the vortex phase as starting conditions, we simulate the evolution of contrail-cirrus. A range of atmospheric conditions and two different aircraft types are considered. Our results show that the initial number of ice crystals and the ambient temperature play a key role in how contrail-cirrus evolve. Fewer initial ice crystals, which may be expected from hydrogen combustion, lead to shorter-lived contrail-cirrus with lower radiative impact. This is mainly because fewer but larger ice crystals fall out of the atmosphere more quickly. We also find that the effect of initial ice crystal number on the radiative impact is not linear, which agrees with findings from earlier research.

1. Introduction

In addition to the climate impact of CO_2 and NO_x emissions, contrails formed behind aircraft can evolve into persistent cirrus clouds under ice supersaturated conditions (Schumann, 2005). These clouds constitute a significant contributor to aviation-induced radiative forcing, accounting for about 57 % of the total net radiative forcing from aviation (Lee et al., 2021). The net radiative impact of contrail-cirrus, reflecting the balance between shortwave cooling and longwave warming, results in a warming of the atmosphere (Burkhardt & Kärcher, 2011; Lee et al., 2021). Climate model studies have demonstrated a substantial reduction in the radiative forcing of contrail-cirrus when the number of nucleated ice crystals is decreased (Bier & Burkhardt, 2022; Burkhardt et al., 2018; Rubin-Zuzic et al., 2025).

Over the past years, there has been a major interest in exploring the feasibility of sustainable aviation fuels (SAFs) and hydrogen (H_2) as alternatives to conventional fossil fuels. Recent measurement campaigns investigating emissions from SAF-powered aircraft have provided valuable insights into the potential to reduce contrail ice crystal numbers. The ECLIF campaigns investigated emissions and contrail formation from aircraft powered by

SAF blends (Bräuer et al., 2021; Dischl et al., 2024; Märkl et al., 2024; Voigt et al., 2021). Because SAF contains fewer aromatic compounds than conventional Jet A-1, combustion produces fewer soot particles (Moore et al., 2017). By probing the exhaust of an Airbus A350-941 aircraft powered by 100% SAF, Märkl et al. (2024) measured a 35% reduction in emitted soot particle number and a 56% decrease in contrail ice crystal number. Moreover, only recently in-flight measurements of contrails produced by H_2 combustion have been conducted within the Blue Condor project (Airbus, 2023). Ice crystal loss during the vortex phase (Kleine et al., 2018; Lewellen, 2014; Unterstrasser, 2014) implies that a reduction in nucleated ice crystals results in a smaller decrease in the number of ice crystals that survive the vortex phase and persist into the dispersion phase (Bier & Burkhardt, 2022; Unterstrasser, 2016).

H_2 combustion and H_2 fuel cells are considered clean propulsion technologies, as they produce neither CO_2 nor soot emissions (Soleymani et al., 2024). H_2 exhibits a specific energy approximately 2.8 times higher than that of conventional kerosene and a water vapor emission index larger by a factor of 7.1. Consequently, the energy-specific emission index of water vapor increases by a factor of around 2.6. As a result, H_2 exhaust plumes reach higher supersaturation levels, and contrails can form at ambient temperatures up to about 10K higher than for kerosene combustion (Bier et al., 2024; Schumann, 1996).

Heat exchange systems in fuel-cell driven aircraft can decrease the exhaust temperature through heat recuperation. Hence, H_2 fuel-cell propulsion can produce a cooler, more humid exhaust than combustion engines. Under these conditions, the plume can reach supersaturations of up to 2,000 %, where homogeneous droplet nucleation becomes possible (Wölk & Strey, 2001), potentially generating large numbers of ice crystals. Because in-flight data are lacking, the relevance of this process in H_2 fuel-cell plumes is still uncertain.

In the absence of soot particles as ice-nucleating sites, other particle types become increasingly relevant for contrail ice crystal formation (Kärcher et al., 2015). In SAF- or H_2-combustion plumes, ultrafine volatile particles may form through nucleation of condensable vapors, such as water vapor and nitric acid, on charged molecular clusters (chemi-ions). These particles are only a few nanometers in size, and they can be emitted in large numbers $\left(\sim 10^{17}\,\mathrm{kg}^{-1}\right)$ (Yu & Turco, 1997). In conventional soot-rich exhaust (soot emission index $EI_s \gtrsim 10^{14}\,\mathrm{kg}^{-1}$), the Kelvin effect suppresses their activation, as ice nucleation preferentially occurs on the larger soot particles. In contrast, under soot-poor $\left(EI_s \lesssim 10^{13}\,\mathrm{kg}^{-1}\right)$ or soot-free conditions, such as those in SAF- or H_2-combustion exhaust, volatile particles can become activated when the plume temperature is well below the Schmidt–Appleman threshold and plume supersaturation is high (Kärcher et al., 2015). In such cases, they may contribute to ice crystal formation, potentially reaching crystal numbers comparable to those in soot-rich regimes (Kärcher & Yu, 2009). Furthermore, lubrication oil particles, as another type of volatile particles, have been demonstrated to act as condensation nuclei in the contrail formation process (Ponsonby et al., 2024). Under soot-poor but oil-rich conditions, oil particles may dominate ice crystal nucleation despite their small size and low hygroscopicity compared to ambient aerosols or soot particles, depending also on engine design (Zink et al., 2025).

In addition to emitted particles, entrained ambient aerosols can influence SAF- and H_2-contrail formation. Bier et al. (2024) modeled an H_2-combustion scenario with ice crystals nucleating exclusively on background aerosols. They conducted sensitivity studies on ambient aerosol number concentration, dry radius, and hygroscopicity. Even with the higher supersaturations present in H_2-exhaust plumes, the resulting ice crystal number concentrations are on the order of 10^{10} to $10^{11}\,\mathrm{m}^{-1}$ for typical ambient aerosol conditions, which corresponds to an 80–90 % reduction compared with kerosene plumes.

Overall, several modeling studies, for example, Burkhardt et al. (2018), Bier et al. (2024), or Rubin-Zuzic et al. (2025), as well as the ECLIF measurement campaigns, demonstrate that reducing the number of emitted particles makes alternative fuel types a promising strategy to mitigate the climate impact of contrail-cirrus. However, the contribution of volatile particles and the potential for homogeneous droplet nucleation under high supersaturation in the context of H_2 propulsion are not yet understood. Hence, we academically explored a wide range of the initially nucleated ice particle number in a previous study that investigated contrail evolution during the vortex phase; the phase in which contrail ice crystals interact with the aircraft's wake vortex system, which lasts a few minutes (Lottermoser & Unterstrasser, 2025). Building upon this prior work, the current study focuses on the further evolution of these young, few-minute-old contrails into aged contrail-cirrus.

Section 2 introduces the model that is used to simulate contrail-cirrus evolution and describes the simulation setup. In Section 3, we examine the impact of various ambient and aircraft-type related parameters on contrail properties. Section 4 presents a comparison of our results with those from other models. The implications of our findings are discussed in Section 5, followed by the conclusions in Section 6.

2. Method

We use the large-eddy simulation (LES) code EULAG-LCM to perform simulations of contrail-cirrus that form behind SAF- or H_2-powered aircraft. The EULAG model is a numerical solver designed for computational fluid dynamics simulations. The Lagrangian Cloud Module (LCM) is coupled to EULAG. LCM includes a Lagrangian particle-tracking method (Sölch & Kärcher, 2010; Unterstrasser & Sölch, 2014), where ice crystals are represented by simulation particles (SIPs), each corresponding to a defined number of ice crystals with identical properties. LCM comprises several microphysical routines, such as the growth of ice crystals due to the deposition of water vapor, latent heat release, or gravitational sedimentation. In this study, we deactivate aggregation and radiation, which is further discussed in Section 5. We assume hexagonal columns for the ice crystal habit. The coupled model version EULAG-LCM has widely been used in previous studies focusing on the contrail evolution during the vortex phase (e.g., Unterstrasser, 2016) and the transition into contrail-cirrus (e.g., Unterstrasser, Gierens, Sölch, & Lainer, 2017; Unterstrasser, Gierens, Sölch, & Wirth, 2017).

Section 2.1 describes the simulation setup. It provides a summary of the vortex phase simulations on which the present study builds (Section 2.1.1) and introduces the simulation parameters used (Section 2.1.2). Section 2.2 defines the quantities analyzed in this study.

2.1. Simulation Setup

In the present study, we apply EULAG-LCM in two dimensions, with x representing the horizontal and z representing the vertical coordinate, that is, the simulation domain is perpendicular to the flight direction. The general setup of the simulations is very similar to previous contrail-cirrus modeling studies with EULAG-LCM (e.g., Unterstrasser, 2020; Unterstrasser, Gierens, Sölch, & Lainer, 2017; Unterstrasser, Gierens, Sölch, & Wirth, 2017). We only provide a brief summary of the basic settings, but describe in detail those aspects that have been adapted and are crucial to the present study.

The domain spans 40.96 or 81.92 km in the x-direction, depending on the strength of vertical wind shear (for higher wind shear values, the contrail spreads faster, and a larger domain is needed), and 2.5 km in the z-direction, representing a portion of the upper troposphere. Using a Cartesian grid, the mesh resolution is 10 m in both horizontal and vertical direction. The simulated time period is 8 hr, with a time step ranging from 0.6 to 2 s, depending on the specific setup.

2.1.1. Hydrogen Parameter Study

Our contrail-cirrus simulations start several minutes after the contrail forms. By this point, the wake vortices have dissipated, and the contrail has a vertical extent of a few hundred meters. The final vertical extent depends on the aircraft type, the initial microphysical properties such as the size of the formed ice crystals, and background conditions, including ambient relative humidity. The simulation results presented in Lottermoser and Unterstrasser (2025), from now abbreviated as LU25VP, serve as a starting point for the contrail-cirrus simulations investigated in this study. In the interest of completeness, we summarize the main findings from LU25VP.

In LU25VP, we presented and analyzed 3D simulations of young contrails, specifically focusing on contrails that form behind H_2-powered aircraft. We modeled the initial minutes of their life cycle, known as the vortex phase, where the interplay of ice microphysics and wake vortex descent and decay is the dominating phenomenon. We performed a total of 150 such simulations (see Table A1 in LU25VP for details), of which 100 are selected for the present study. Each defines an initial state of a contrail-cirrus simulation.

We investigated the sensitivity of H_2-contrail properties to ambient and aircraft-dependent parameters with particular emphasis on the number of ice crystals surviving adiabatic heating during the vortex descent. By varying the initial number of ice crystals and the emitted water vapor mass, we modeled a potential H_2-propulsion scenario. Specifically, we systematically scaled the initial ice crystal number, N_{00}, up and down by factors of 10 and 100, resulting in a range of 10^{10} to 10^{14} ice crystals per meter. The N_{00}-downscaling scenarios simulate a

Table 1
Ice Crystal Parameters Used as Input for the Vortex Phase Simulations Presented in Lottermoser and Unterstrasser (2025)[a]

	A320/B737	A350/B777
$N_{00}/\left(\left[10^{10}, 10^{11}, 10^{12}, 10^{13}, 10^{14}\right]/\mathrm{m}^{-1}\right)$	0.85	3.38
$I_{00}/(10^{-3}\ \mathrm{kg\ m}^{-1})$	[3.7, 9.5]	[15.0, 38.6]

[a]N_{00} and I_{00} represent the initial ice crystal number and initial water vapor emission, respectively (prior to ice crystal loss during the vortex phase). The $N_{00} \sim 10^{12}\ \mathrm{m}^{-1}$ case is the default. High-N_{00} and low-N_{00} cases refer to the N_{00}-upscaling $\left(N_{00} \gtrsim 10^{13}\ \mathrm{m}^{-1}\right)$ and N_{00}-downscaling $\left(N_{00} \lesssim 10^{11}\ \mathrm{m}^{-1}\right)$ scenarios, respectively. In the second row, the numbers in brackets correspond to $I_{00,\mathrm{kero}}$ and $I_{00,\mathrm{H_2}}$, respectively.

potential SAF- or H_2-combustion setup, where fewer ice crystals form due to the reduction or absence of soot particle emissions, respectively (Bier et al., 2024; Voigt et al., 2021). The lower bound of 10^{10} ice crystals per meter is informed by simulation results of Bier et al. (2024) (see Section 1). Conversely, the N_{00}-upscaling simulations account for alternative ice crystal formation processes in soot-poor or soot-free scenarios, including the potentially significant contribution of volatile particles to the ice nucleation process. In a box model study investigating the role of lubrication oil particles in the soot-poor and H_2-combustion scenario, Zink et al. (2025) showed that, at low ambient temperatures, final ice crystal number concentrations may reach up to $10^{14}\ \mathrm{m}^{-1}$ when the oil emission index is on the order of $10^{17}\ \mathrm{kg}^{-1}$. Moreover, homogeneous droplet nucleation in fuel cell exhausts could similarly generate a high ice crystal number, justifying the upper limit of N_{00} in our simulations.

The increase in water vapor emission, I_{00}, when switching to H_2 results from the differing fuel properties of H_2 and kerosene and is incorporated by multiplying the default kerosene value by a factor of 2.57 (see Section 1). I_{00} of the kerosene and hydrogen scenarios are denoted by $I_{00,\mathrm{kero}}$ and $I_{00,\mathrm{H_2}}$, respectively. The ice crystal properties used as input for the vortex phase simulations are listed in Table 1. The water vapor emission index in the SAF case can be up to 10 % higher than in the kerosene case due to the increased hydrogen content of SAF (Dischl et al., 2024; Teoh et al., 2022). However, our results presented in Section 3 indicate that contrail properties are only weakly sensitive to I_{00}. Therefore, simulations using $I_{00,\mathrm{kero}}$ and the proposed range of N_{00} values can be likewise interpreted as SAF scenarios, whereas simulations with $I_{00,\mathrm{H_2}}$ exclusively represent H_2 propulsion setups. Although I_{00} and N_{00} are not independent variables, as the number of initially formed ice crystals can depend on the water vapor emission, we prefer to vary I_{00} and N_{00} independently from each other within the chosen parameter range. This allows us to disentangle the effects that variations of I_{00} and N_{00} have on the subsequent contrail phases.

In LU25VP, we examined two aircraft types: an A350/B777-like aircraft with a wingspan of 60.3 m, representing a typical widebody aircraft and used as the default case, and a smaller A320/B737-like aircraft with a wingspan of 34.4 m as an example of a narrowbody aircraft. As noted in LU25VP, default values for N_{00} and I_{00} for these two aircraft were taken from Unterstrasser and Görsch (2014). We emphasize that some parameters, such as fuel consumption or wingspan, may not exactly reflect current aircraft specifications. Throughout this study, references to "A350" or "A320" should be understood as shorthand for "A350/B777-like aircraft" or "A320/B737-like aircraft," respectively. The inclusion of the smaller aircraft into our study accounts for the potential earlier adoption of H_2 propulsion in regional aviation. We varied the ambient temperature at cruise altitude between 217 and 235 K, with 217 K as the default value based on cruise temperature statistics (e.g., Kärcher et al., 2009). The upper temperature limit reflects the possibility that contrails from H_2-powered aircraft can form in warmer conditions where those from conventional kerosene combustion typically do not. The chosen temperature range corresponds to cruise-altitude pressure values between 233 and 235 hPa. Additionally, the ambient relative humidity with respect to ice was set to either 110% or 120%, informed by measurements (Iwabuchi et al., 2012; Petzold et al., 2020). The extent of ice crystal loss may substantially differ between these two cases (see, e.g., Figure 1 in Unterstrasser (2014)). We then define the survival fraction as the final number of ice crystals surviving the vortex phase N_0 divided by the initial ice crystal number N_{00}.

The main findings in LU25VP are the following:

1. We observe survival fractions of up to 90%–100% if N_{00} is downscaled. This is due to the larger crystal sizes compared to the N_{00}-reference or -upscaling cases.
2. Simulations with $I_{00} = I_{00,\mathrm{H_2}}$ show higher survival fractions compared to the default $I_{00,\mathrm{kero}}$ cases, as the additional water vapor increases the initial average crystal sizes. This finding holds for all N_{00} variations.
3. The impact of adiabatic heating in the downward moving vortex system on the ice crystals increases with increasing ambient temperature. Therefore, survival fractions decrease with higher cruise-altitude temperatures for all N_{00} scenarios, with the strongest losses for temperatures higher than 230 K.
4. Compared to the default ambient relative humidity of 120%, simulations with a lower value of 110% consistently show stronger sublimation and reduced vertical extents of contrails across all N_{00} scenarios.

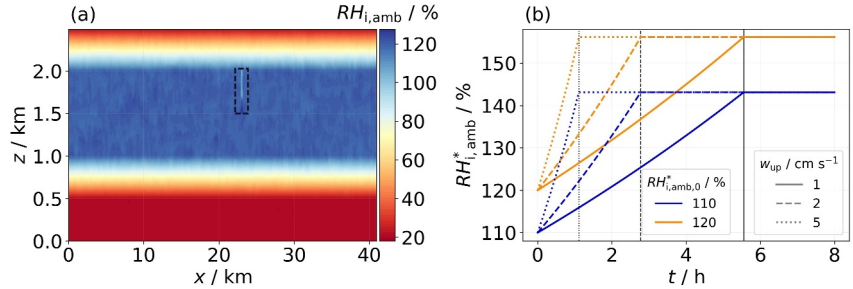

Figure 1. Vertical profile of relative humidity with respect to ice (panel a). The black box frames the initial position of the contrail. Evolution of relative humidity with respect to ice at $z = 2$ km for different updraught speeds w_{up} (panel b). The black lines mark the end points of the uplifting process.

In summary, we find the initial differences in ice crystal number, encompassing four orders of magnitude, are reduced to three or even two orders of magnitude, depending on the initial ice crystal properties and the prescribed ambient conditions. Table A1 presents the final total number N_0 and mass I_0 of the contrails after the vortex phase that are used as input for the present contrail-cirrus study.

2.1.2. Contrail Initialization and Simulation Parameters

To initialize the contrail and the background fields, the Eulerian 3D data, such as perturbations in water vapor concentration and potential temperature, are averaged along the flight direction and interpolated onto the coarser grid. The SIPs representing the ice crystals are merged to reduce their overall number. The initialized contrails are described by approximately 10^5 SIPs, which have been shown to provide robust estimates of the contrail quantities analyzed in the present study.

Figure 1a illustrates an example initialization setup, with the black box encompassing the region where the contrail from the 3D vortex phase simulation is embedded. In this example, the contrail is located at $x \approx 23$ km and has a vertical extent of around 500 m. The flight altitude in the simulation domain is at $z = 2000$ m. This value should not be interpreted as a real flight altitude; it is only a vertical coordinate within the model domain. The prescribed temperature and pressure correspond to upper-tropospheric cruise conditions. For each contrail-cirrus simulation, we conduct four different realizations of the same setup by horizontally shifting the contrail position relative to the background, as indicated by the black box in Figure 1a. With this, we ensure that we account for a potentially different contrail evolution due to small turbulence-induced perturbations in the background fields. Unless stated, we average over the four simulations and compute mean contrail quantities.

Figure 1a also displays the initially prescribed vertical profile of ambient relative humidity with respect to ice, $RH_{i,amb}$, which we set to either 110 % or 120 % within the ice supersaturated layer (ISSL). We denote this initial value as $RH^*_{i,amb,0}$. The ISSL has an initial thickness $d_{ISSL,0}$ of roughly 1,100 m ($RH^*_{i,amb,0} = 110\%$) or 1,180 m ($RH^*_{i,amb,0} = 120\%$), transitioning linearly to subsaturated layers with 20% relative humidity at the top and bottom parts of the simulation domain. In the ISSL, the local humidity values fluctuate around the prescribed $RH^*_{i,amb}$ value. Furthermore, RH_i inside the contrail is lower than the background humidity as the contrail ice crystals have already depleted water vapor in this area (LU25VP).

The background relative humidity is not static in our simulation. $RH_{i,amb}$ changes during the simulation as we prescribe a spatially homogeneous updraught of the whole domain over a certain time period. This updraught motion induces adiabatic cooling, which is represented by an external forcing term in the temperature equation in EULAG (a more technical description is given in Section 2 of Unterstrasser and Gierens (2010b)). We consider three different updraught scenarios with updraught velocities $w_{up} = 1$, 2, or 5 cm s^{-1} (referred to as low, medium, high). Previous contrail-cirrus simulations have demonstrated that this parameter influences the contrail evolution (Lewellen, 2014; Unterstrasser, 2020; Unterstrasser, Gierens, Sölch, & Wirth, 2017). To achieve a final adiabatic cooling ΔT_{cool} of 2 K (corresponding to a vertical displacement of ≈200 m), we terminate the uplift motion by prescribing fixed uplift durations. Faster updraughts correspond to shorter uplift times, as illustrated in Figure 1b. The uplift velocities of 1, 2, and 5 cm s^{-1} yield uplift durations of 20000, 10000, and 4000 s, which are denoted by the vertical black lines. The cooling by 2 K causes $RH^*_{i,amb}$ to reach final values of 143% in the case of

Table 2
Numerical and Atmospheric Parameters Used in Our Simulations[a]

Numerical parameters	
L_x, L_z/m	40960 (81920), 2500
dx, dz/m	10, 10
t_{sim}/hr	8
dt/s	0.6, 1, 1.25, 2
Atmospheric parameters	
N_{BV}/s^{-1}	0.01
$RH^*_{i,amb,0}$/%	110, 120*
T_{CA}/K	217*, 225, 230, 233, 235
ΔT_{cool}/K	2
$d_{ISSL,0}(110\%), d_{ISSL,final}(110\%)$/m	1100, 1350
$d_{ISSL,0}(120\%), d_{ISSL,final}(120\%)$/m	1180, 1410
w_{up}/cm s^{-1}	1*, 2, 5
s/s^{-1}	0.002*, 0.006

[a]L_x, L_z: domain dimension in horizontal and vertical direction (the domain size in horizontal direction is doubled in the high-shear cases); dx, dz: mesh size in horizontal and vertical direction; t_{sim}: total simulated time; dt: time step; N_{BV}: Brunt-Väisälä frequency; $RH^*_{i,amb,0}$: initial ice relative humidity in the supersaturated layer; T_{CA}: initial ambient temperature at flight level; ΔT: final adiabatic cooling; $d_{ISSL,0}$, $d_{ISSL,final}$ (x %): thickness of the ice supersaturated layer at the beginning and end of the simulation (the value in brackets specifies $RH^*_{i,amb,0}$); w_{up}: updraught speed; s: vertical wind shear. Values marked with an asterisk indicate the baseline values.

$RH^*_{i,amb,0} = 110\%$ and 156% for $RH^*_{i,amb,0} = 120\%$. Hence, the thickness of the ISSL increases to $d_{ISSL,final}$ = 1,350 m ($RH^*_{i,amb,0}$ = 110 %) or 1,410 m ($RH^*_{i,amb,0} = 120\%$).

For an ambient supersaturation above a critical threshold, natural cirrus can form via heterogeneous and/or homogeneous nucleation (Cziczo et al., 2013; Gierens, 2003; Koop et al., 2000). We deliberately deactivate both nucleation pathways and therefore suppress the formation of natural cirrus at later contrail stages. Hence, we focus on simulating contrails evolving into aircraft-induced contrail-cirrus in an otherwise cloud-free atmosphere. A discussion of this assumption is deferred to Section 5.

We vary the ambient temperature at flight altitude: T_{CA} = 217, 225, 230, 233, and 235 K. Throughout the text, T_{CA} represents the initial temperature at cruise altitude. The vertical temperature profiles are characteristic of a stably stratified atmosphere, with a Brunt-Väisälä frequency N_{BV} of 0.01 s^{-1}, a typical value of the upper troposphere. Background turbulent velocity fields were derived from a-priori simulations with a root mean square value of approximately 0.12 m s^{-1} (Unterstrasser, 2020; Unterstrasser, Gierens, Sölch, & Lainer, 2017). Furthermore, we prescribe vertical wind shear, $s = \frac{\partial u}{\partial z}$, which is defined as the vertical gradient of the horizontal wind field. For simulations with w_{up} = 1, 2, and 5 cm s^{-1}, we apply a moderate shear value of s = 0.002 s^{-1}. We additionally consider a higher shear value of 0.006 s^{-1} for simulations with w_{up} = 1 cm s^{-1}.

Table 2 provides a summary of the setup parameters. Based on the 100 vortex phase simulations, we conducted 1,600 contrail-cirrus simulations, covering four meteorological scenarios (three w_{up} values and one additional high wind shear scenario) and four initial contrail positions. Even though temperature is also a meteorological variable, our meteorological scenarios are, by definition, solely characterized by w_{up} and s. This appears reasonable as the encountered ambient temperature depends, apart from the prevailing meteorological conditions, even more strongly on the flight altitude. While the total number of simulations amounts to 1,600, the variation in initial contrail position does not alter the underlying parameter configuration. Therefore, these cases are considered repetitions under identical parameter settings. As such, we effectively conducted 400 distinct parameter simulations.

2.2. Quantities of Interest

This section introduces the key quantities used throughout the study.

The total ice crystal number N_{tot} (in units m^{-1}) is defined as the 2D spatial integral of the ice crystal concentration N (in units m^{-3})

$$N_{tot}(t) = \int\int N(x,z,t)\,\mathrm{d}x\,\mathrm{d}z, \tag{1}$$

and, analogously, the total ice mass M_{tot} (in units kg m^{-1}) is the 2D spatial integral of the ice water concentration IWC (in units kg m^{-3})

$$M_{tot}(t) = \int\int IWC(x,z,t)\,\mathrm{d}x\,\mathrm{d}z, \tag{2}$$

where IWC is the first moment of the lognormal mass distribution prescribed in our model (e.g., Unterstrasser, 2014). The normalized number of ice crystals $f_N(t)$ is defined as the number of ice crystals $N_{tot}(t)$ divided by the initial ice crystal number of the dispersion phase $N_0 = N_{tot}(t = 0)$. Analogously, the normalized number

of sublimated ice crystals $f_{N,\mathrm{subl}}(t)$ is the number of sublimated ice crystals divided by N_0. This quantity can be further subdivided into $f_{N,\mathrm{subl,in\ situ}}(t)$, representing losses due to in situ sublimation, and $f_{N,\mathrm{sedi}}(t)$, representing sedimentation losses.

The vertical profiles of contrail ice crystal number N_v and ice mass M_v are

$$N_\mathrm{v}(z,t) = \int N(x,z,t)\,\mathrm{d}x \tag{3}$$

and

$$M_\mathrm{v}(z,t) = \int IWC(x,z,t)\,\mathrm{d}x. \tag{4}$$

Vertical profiles of f_N and $f_{N,\mathrm{subl}}$ are denoted by $f_{N,\mathrm{v}}$ and $f_{N,\mathrm{v,subl}}$, respectively.

We further define the size D of an ice crystal, where its mass and area are derived via mass-size and area-size relationships for hexagonal columns (Sölch & Kärcher, 2010). We calculate the effective crystal diameter d_eff according to Yang et al. (2000), where the summed particle volume V_tot and summed particle projected area A_tot are used:

$$d_\mathrm{eff} = \frac{3}{2}\frac{V_\mathrm{tot}}{A_\mathrm{tot}}. \tag{5}$$

While the size D represents the maximum dimension of a single ice crystal, and ice particle size distributions are derived in terms of D, the effective diameter d_eff is a measure of an ice crystal population and is employed in radiative transfer calculations or in remote sensing applications (McFarquhar & Heymsfield, 1998; Schumann et al., 2011).

An important quantity in the context of the contrail's radiative properties is the optical thickness τ, which is the vertically integrated extinction coefficient χ:

$$\tau(x,t) = \int \chi(x,z,t)\,\mathrm{d}z. \tag{6}$$

The extinction coefficient is calculated as the projected area of all ice crystals in each grid box multiplied by the extinction efficiency, Q_ext. In this study, we apply a constant value of $Q_\mathrm{ext} = 2$. This choice is strictly valid only in the geometric optics limit, that is, when the size parameter is much larger than one (typically $\gtrsim 20$ to 30) (Hansen & Travis, 1974). In this regime, where ice crystal sizes are much larger than the wavelength (e.g., 2 to 4 μm for visible wavelengths), Q_ext approaches 2. For smaller crystals, such as in our N_{00}-upscaling case, where the size parameter is closer to unity, Mie scattering occurs and Q_ext oscillates around 2 (van de Hulst, 1981). We therefore acknowledge that applying a constant value represents a simplified assumption. On the other hand, using a constant Q_ext value in our evaluation has the advantage that χ and d_eff depend only on the ice crystal habit and size distribution as modeled with EULAG-LCM and not on further processes like Mie scattering. Hence, those quantities are easier to interpret.

The mean optical thickness $\tau_\mathrm{m}(t)$ is computed as the average of $\tau(x,t)$, excluding columns where $\tau(x,t) < 0.005$. Also, we define the contrail's optical width τ_hor, which is written as

$$\tau_\mathrm{hor}(z,t) = \int \chi(x,z,t)\,\mathrm{d}x. \tag{7}$$

Further, the total extinction E reads as

$$E(t) = \int\int \chi(x,z,t)\,\mathrm{d}x\,\mathrm{d}z = \int \tau(x,t)\,\mathrm{d}x. \tag{8}$$

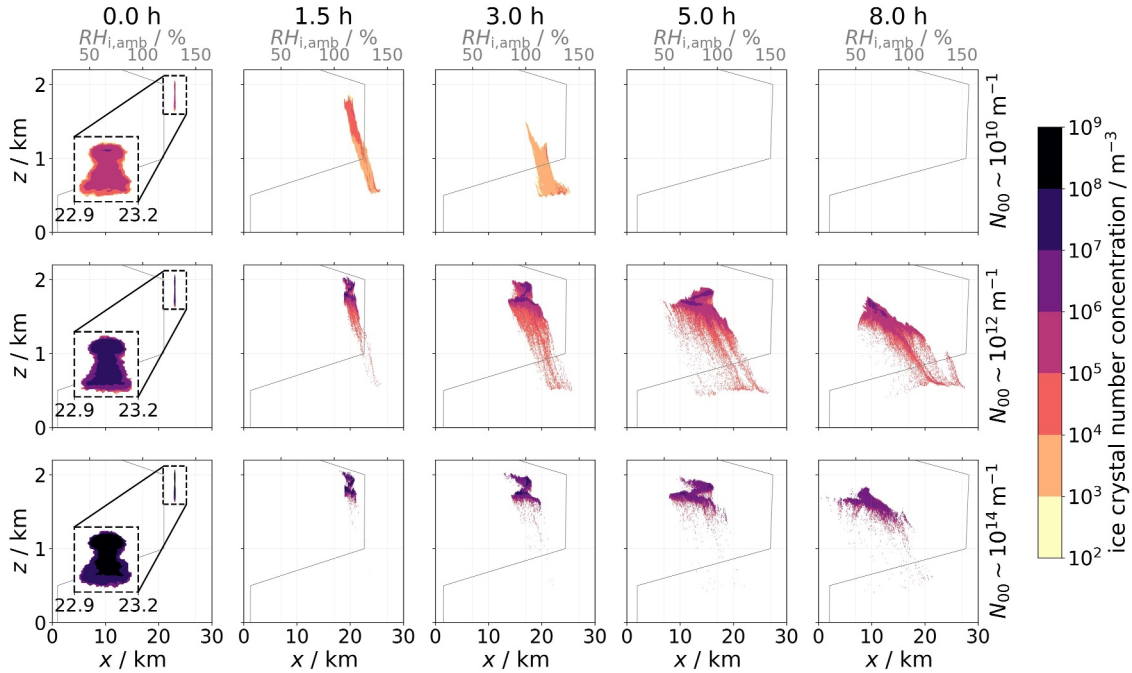

Figure 2. Ice crystal number concentration in the (x, z)-plane at five different time steps (columns). For better visibility, the initial contrail (first column) is magnified, enlarging the region from 22.9 to 23.2 km. The rows show results for a different initial ice crystal number N_{00}: The middle row represents the reference N_{00} case, while the upper and lower rows correspond to the factor-of-100 N_{00}-downscaling and N_{00}-upscaling simulations, respectively. The background relative humidity profile is displayed as a gray curve in each panel. Note that only a fraction of the simulation domain is depicted.

The time-integrated total extinction $\hat{E}$ is

$$\hat{E} = \int_0^{t_{\text{lim}}} E(t)\,\mathrm{d}t, \tag{9}$$

which represents the cumulative effect of total extinction over the simulation period up to t_{lim}, capturing the overall radiative impact of the contrail.

3. Results

This section presents example contrail-cirrus simulations as an introductory part (Section 3.1) before progressing to the parameter study of contrail-cirrus properties (Section 3.2). With a focus on the N_{00}-sensitivity, Section 3.1 illustrates the fundamental physical processes during contrail-cirrus evolution, including cross-sectional area evolution (Section 3.1.1), ice crystal loss processes (Section 3.1.2), and the temporal evolution of integrated contrail properties (Section 3.1.3). Section 3.2 analyzes how specific parameter variations influence the contrail-cirrus evolution (Section 3.2.1), examines a scaling relation between E and N_{00} (Section 3.2.2), investigates the response of $\hat{E}$ to N_{00} in terms of t_{lim} and T_{CA} (Section 3.2.3), and evaluates the sensitivity of $\hat{E}$ to N_{00} across all parameter variations (Section 3.2.4).

3.1. Impact of Initial Ice Crystal Number Scaling on Contrail-Cirrus Evolution: Example Simulations

The example simulations feature an A350/B777-like aircraft with an initial water vapor emission of 38.6 g m^{-1}, representing H_2 propulsion (see Table 1). We set the ambient conditions to the baseline values described in Table 2. Based on Figures 2–5, we explain important processes involved in contrail-cirrus evolution that have been explored in previous studies (Lewellen, 2014; Lewellen et al., 2014; Unterstrasser & Gierens, 2010a, 2010b; Unterstrasser, Gierens, Sölch, & Lainer, 2017). Expanding upon these findings, our study investigates the impact of the initial ice crystal number varied over a broad range.

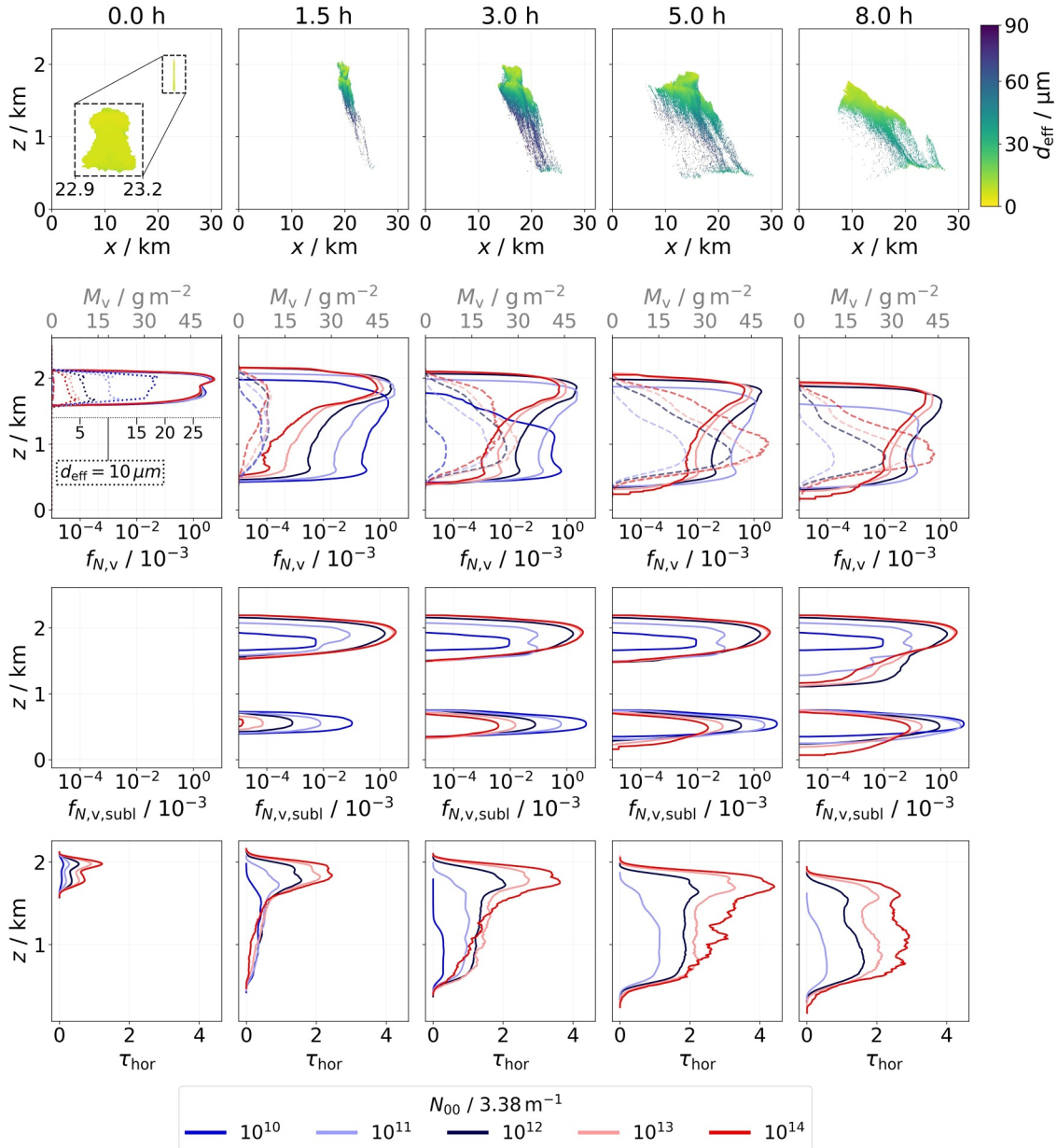

Figure 3. First row: temporal evolution of effective ice crystal diameter in the (x, z)-plane. Note that the d_{eff} values of the N_{00}-reference simulation are shown here. Second row: vertical profiles of ice mass (dashed) and normalized ice crystal number (solid) for the scaled initial ice crystal number (color). At $t = 0$ h, we also display the initial effective diameter (dotted). Third row: vertical profiles of normalized number of sublimated ice crystals. Fourth row: vertical profiles of optical width. The time steps are the same as for Figure 2. The shown results correspond to the baseline simulation setup (see Table 2).

3.1.1. Low- and High-N_{00} Contrails: Implications on the Cross-Sectional Areas

Figure 2 illustrates the temporal evolution of ice crystal number concentration. During the first hour, contrail tilting due to vertical wind shear is apparent, while entrainment of supersaturated air promotes the growth of the ice crystals. The development of fallstreaks through sedimentation (most clearly seen in the middle row of Figure 2) creates two distinct regions: a compact core with high ice crystal number concentrations and an expanding area dominated by sparsely populated fallstreaks. The distribution of ice crystal sizes differs between the core and the fallstreaks: Figure 3 shows large ice crystals with diameters up to 100 µm in the fallstreaks, consistent with observations by Lawson et al. (1998). In contrast, small crystals with sizes 10–20 µm are present in the core, as reported by Voigt et al. (2017) and Wang et al. (2023).

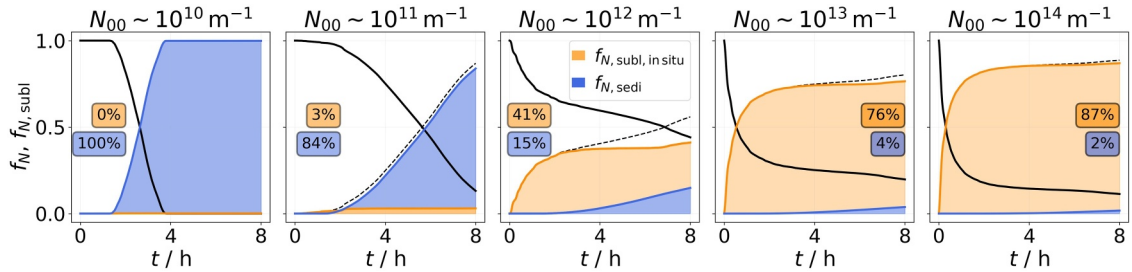

Figure 4. Temporal evolution of normalized number of ice crystals (solid black) and sublimated ice crystals (dashed black), where the latter is further subdivided into in situ sublimation (orange) and sedimentation (blue). The columns represent the five N_{00}-scaling cases of the baseline simulation setup (see Table 2). The percentage values in the orange (blue) boxes indicate the final fraction of ice crystals lost due to in situ sublimation (sedimentation).

The evolution of contrail-cirrus differs significantly across the N_{00} scaling simulations. Comparing the first and third rows in Figure 2, a well-developed fallstreak emerges within 1.5 hr in the $N_{00} \sim 10^{10}\,m^{-1}$ scenario, whereas the $N_{00} \sim 10^{14}\,m^{-1}$ contrail retains a distinct core with relatively weak crystal settling. The low-N_{00} contrail dissipates after just 3–4 hr. These observations are attributed to the varying crystal sizes between both scenarios, as further examined in the following section.

3.1.2. Low- and High-N_{00} Contrails: Sedimentation Versus In Situ Sublimation

Two primary mechanisms are responsible for the loss of ice crystals during contrail-cirrus evolution (Unterstrasser, Gierens, Sölch, & Lainer, 2017): in situ sublimation, which occurs when local humidity fluctuations induce transiently subsaturated air masses, leading to the preferential sublimation of smaller ice crystals due to the Kelvin effect (Lewellen, 2012); and sedimentation loss, where ice crystals fall into subsaturated air beneath (in our scenarios, this is the region $z \leq 700$–800 m), and sublimate. Although those ice crystals are ultimately lost due to sublimation, we refer to this as sedimentation loss.

The impact of sedimentation varies across the different N_{00} cases. Initially, ice crystals are larger in low-N_{00} contrails (10–20 μm) and smaller in high-N_{00} contrails (3–4 μm, see dotted lines in Figure 3, first panel in the

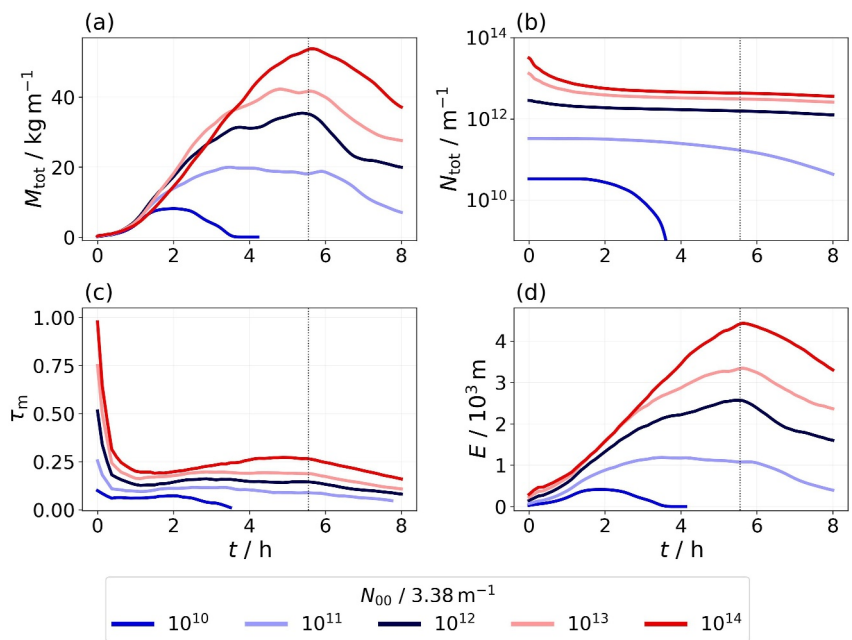

Figure 5. Temporal evolution of the total ice mass (a), total ice crystal number (b), mean optical thickness (c), and total extinction (d) of the baseline simulation setup. The vertical black lines indicate the time point where the updraught motion stops. Colors indicate the N_{00} scaling.

second row), influencing their sedimentation behavior. The fallstreaks become increasingly populated over time across all N_{00} scenarios, redistributing ice mass toward lower altitudes (Figure 3, second row). However, in low-N_{00} cases, the sedimentation flux of ice crystal number and mass becomes substantial within the first 1–2 hr, leading to a fast dehydration of the contrail core. Considering the normalized number of sublimated ice crystals, $f_{N,\mathrm{subl}}$, in the third row, two distinct vertical sublimation peaks arise: one peak covering the contrail core and representing the in situ losses, and one peak at lower altitudes in the subsaturated layer representing the sedimentation losses in the fallstreaks. Apparently, the order of the colors representing the N_{00} parameter is reversed in the two peaks: In low-N_{00} contrails, the ice crystals predominantly get lost by sedimentation processes, whereas the major part of ice crystals sublimate at higher altitudes in high-N_{00} contrails.

To further support this finding, Figure 4 depicts the normalized number of ice crystals (solid black) and the normalized number of sublimated ice crystals (dashed black) for the different N_{00}-scaling scenarios. In the downscaling cases, sedimentation loss approaches or reaches 100 %, whereas in the upscaling cases, it is nearly negligible ($\lesssim$4%). Instead, crystal loss in the high-N_{00} cases, where ice crystals are on average smaller (Figure 8), is primarily driven by in situ sublimation ($\gtrsim$76%), which is in turn absent or minimal in the low-N_{00} cases ($\lesssim$3%). Notably, when going from $N_{00} \sim 10^{12}\,\mathrm{m}^{-1}$ to $N_{00} \sim 10^{14}\,\mathrm{m}^{-1}$, the in situ loss rate strongly increases from 41% to 87%, as the smallest ice crystals sublimate almost immediately. This is confirmed by the evolving size spectra, displayed in the first row of Figure 8 ($T_{\mathrm{CA}} = 217\,\mathrm{K}$), showing that the size spectrum shifts toward larger crystal sizes over time across all N_{00} scalings: Small crystals sublimate in situ, and large crystals grow at the expense of smaller ones—a process known as Ostwald ripening (Lewellen, 2012). A "fallstreak shoulder" appears earlier in the N_{00} downscaling scenarios (blue curves), while a more pronounced "sublimation tail" is observed in the upscaling cases (red curves) over the entire period.

Notably, the colored pattern of Figure 4 remains largely unchanged when varying temperature or updraught speed (not shown). Thus, sedimentation emerges as the dominant factor governing the shorter lifetime of low-N_{00} contrail-cirrus compared to their high-N_{00} counterparts. The initial onset of sedimentation is similar across the N_{00} cases (after $\approx$ 70 min). It depends more strongly on ambient temperature and relative humidity. We find an earlier onset of fallstreak growth in warm cases, after $\approx$ 25 min for $T_{\mathrm{CA}} = 235\,\mathrm{K}$, which was also found by Lewellen et al. (2014).

These findings have strong implications on the temporal evolution of optical width τ_{hor}, shown in the fourth row in Figure 3. Evident in all scaling simulations, τ_{hor} of the fallstreaks increases over time due to the increasing number and mass of ice crystals there, whereas in the core region τ_{hor} first increases but then decreases again. Due to the steady supply of ambient water vapor in updraught scenarios and contrail spreading, ice crystals keep growing, and sedimentation losses become more substantial, eventually outweighing the deposition-induced mass increase in the core region. These processes happen earlier in the low-N_{00} contrails, which are characterized by relatively greater sedimentation fluxes. In these cases, the extinction in the fallstreaks reaches levels comparable to those in the contrail core after just 1–3 hr. On the other hand, a high number of initial ice crystals corresponds to a large projected area density and, hence, a greater extinction of radiation. Therefore, the overall larger values of τ_{hor} observed in the high-N_{00} scenarios are expected. In these scenarios, the peak optical width continues to increase as long as the updraught motion persists.

3.1.3. Low- and High-N_{00} Contrails: Temporal Evolution of Contrail Properties

Lastly, we examine the temporal evolution of important contrail-cirrus properties, including total ice crystal number, total ice mass, mean optical thickness, and total extinction, see Figure 5. M_{tot} and E increase with the entrainment of moist air, sustaining crystal growth as long as the updraught persists. However, once the updraught ceases (in this example case, at 5.5 hr), the crystal growth halts and can no longer compensate for sedimentation and in situ losses. While the rate of change remains comparable for cases with $N_{00} \geq 10^{12}\,\mathrm{m}^{-1}$, a noticeable flattening of ice mass and total extinction occurs earlier in the $N_{00} \sim 10^{11}\,\mathrm{m}^{-1}$ and $N_{00} \sim 10^{10}\,\mathrm{m}^{-1}$ scenarios already after 2 and 1 hr, respectively, due to the rapid sedimentation of ice crystals in these cases. The sensitivity of N_{tot} to N_{00} is asymmetrical, as also found by Lewellen et al. (2014): For $N_{00} \geq 10^{12}\,\mathrm{m}^{-1}$, the initial difference of a factor of 11 diminishes to a factor of 3 over time, whereas for $N_{00} < 10^{12}\,\mathrm{m}^{-1}$, the difference in N_{tot} increases. Note that the initial factor of 10^4 difference (N_{00}) diminishes to 10^2 (N_0), highlighting the importance of accounting for vortex phase losses as outlined in LU25VP. Within the first 30 min, τ_{m} drops due to contrail broadening (the relative change of contrail width is largest for the initially narrow contrails). After this initial

drop, the ice crystal growth can overcompensate the ongoing shear-induced spreading, leading to an increase of τ_m as observed for cases with $N_{00} \geq 10^{12}$ m^{-1}. The peaks of M_{tot} and E roughly coincide in time. In contrast, τ_m stays constant or monotonically decreases for low-N_{00} contrail-cirrus as the crystal growth cannot compensate for the continuous loss of sedimenting ice crystals and the shear-induced spreading.

This section has demonstrated that the N_{00} value is a key parameter with a lasting impact on the overall properties and lifetime of contrail-cirrus. The example simulations presented so far showcase the relative contributions of in situ sublimation and sedimentation loss across the N_{00}-scaling scenarios. For example, the rapid and intense sedimentation loss in the extreme low-N_{00} case (e.g., leftmost panel in Figure 4 or dark blue curves in Figure 5) leads to contrail dissipation within 3–4 hr. This already suggests a great potential of reducing the initial ice crystal number for the purpose of reducing the contrail-cirrus radiative impact.

3.2. Parameter Study of Contrail-Cirrus Properties

This section aims to answer the question of how the relative differences between the N_{00} scenarios qualitatively change for variations in aircraft type and water vapor emission, as well as for variations in ambient conditions, such as ambient temperature, relative humidity, updraught speed, and vertical wind shear.

3.2.1. Impact of Parameter Variations on Contrail-Cirrus Properties

Figures 6 and 7 show sample cross-sections, with each column representing a specific parameter variation around a baseline state as described in Section 2.1. The contrail-cirrus properties shown in Figure 5, total ice mass, total ice crystal number, total extinction, and mean optical thickness, are displayed row-wise.

In general, variations in relative humidity or temperature affect the number of ice crystals surviving the vortex phase and the contrail vertical extent, which in turn influence the initialization of the dispersion phase. Updraught speed w_{up} and vertical wind shear s are only varied in the contrail-cirrus simulations. Hence, all simulations that vary only w_{up} or s are initialized with identical contrails.

First, we examine variations in aircraft- and fuel-related parameters. A variation in the initial water vapor mass, shown in Figure 6a, has only a minor impact on contrail-cirrus evolution: In the case of a higher water vapor emission (solid lines), the slightly larger values of total ice mass, total extinction, and optical thickness result from the higher survival fraction of ice crystals during the vortex phase, which was shown in Section 3.4 of LU25VP. Thus, the slight differences in the evolution of "I_{00,H_2}"- and "$I_{00,kero}$"- contrails stem from differences in N_0 rather than I_{00}. Switching from an A350 aircraft to a smaller A320 aircraft results in notable differences in the evolution of total contrail properties (b). The lower peak ice mass, peak total extinction, and peak optical thickness in the A320 case compared to the A350 case can be attributed to two main factors. On the one hand, the A320 contrail is shallower after the vortex phase, leading to less spreading and reduced water vapor uptake during the contrail-cirrus evolution. On the other hand, although ice crystal number reduction during the vortex phase is less pronounced in the A320 case compared to the A350 case (LU25VP), the A320 aircraft has a smaller N_{00} value (roughly one fourth, see Table 1), which leads to a smaller N_0 value, and, therefore, to smaller peak values of ice mass, crystal number, and extinction.

Second, we analyze variations of ambient conditions, as shown in Figure 7. A variation of updraught speed is displayed in (a). Previous studies have shown that strong but short-lasting updraughts shorten contrail lifetimes, as ice crystals grow rapidly early on but then quickly sediment (Unterstrasser & Gierens, 2010b; Unterstrasser, Gierens, Sölch, & Wirth, 2017). Consistent with this, we observe a $\lesssim$10 min earlier onset of sedimentation-induced ice crystal loss in the high-updraught cases across all parameter variations. Although initially unexpected, ice crystal loss due to in situ sublimation ultimately dominates in high-updraught scenarios. This is explained by the short uplift period of around 1 hr: Once the updraught ceases, no additional water vapor is available, leading to in situ sublimation. In the low-updraught scenarios, by contrast, additional moisture becomes available for roughly 5.5 hr, yet at a lower rate. This leads to a larger fraction of ice crystals that get lost by sedimentation.

The strength of vertical wind shear plays a crucial role in contrail-cirrus evolution (b). High wind shear leads to rapid contrail broadening and enhances ice crystal growth by continuously transporting them horizontally into regions with undepleted, supersaturated air. This results in a substantial increase in ice mass and extinction—

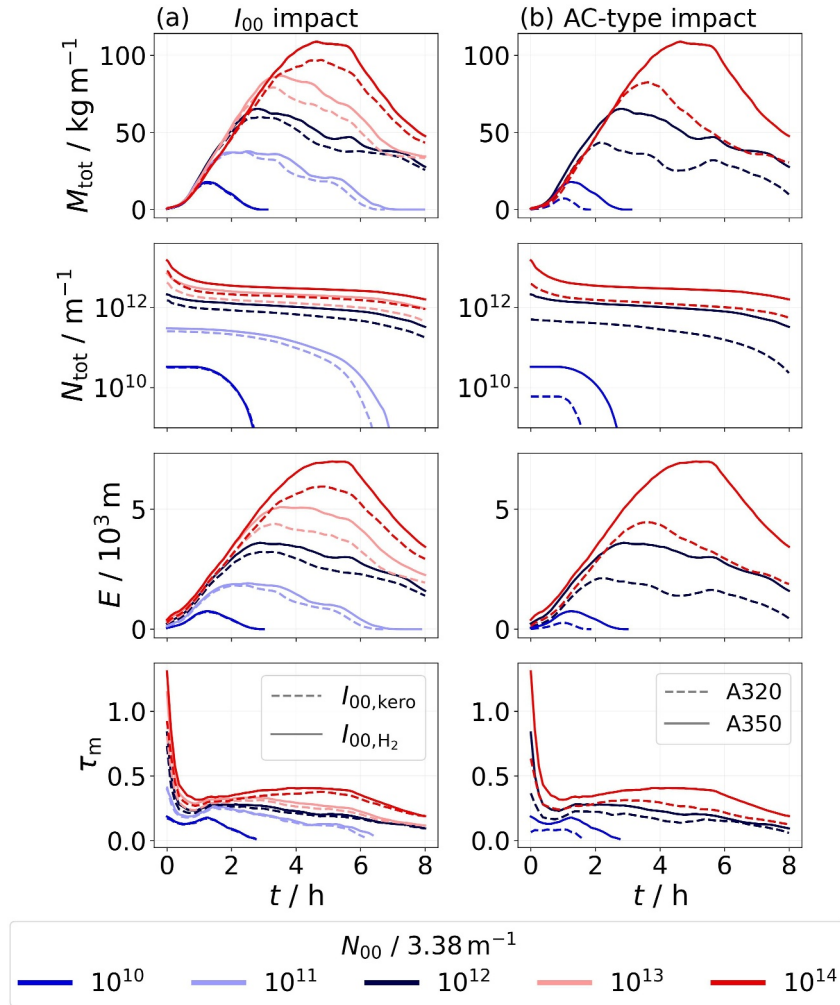

Figure 6. Temporal evolution of total ice mass, total ice crystal number, total extinction, and mean optical thickness depending on the N_{00} scaling, denoted by the colors. Baseline state: A350 aircraft with water vapor emissions characteristic of H_2 propulsion at $RH^*_{i,amb,0} = 120\,\%$ and $T_{CA} = 225\,K$, with a meteorological scenario of $w_{up} = 1\,cm\,s^{-1}$ and $s = 0.002\,s^{-1}$. *Column a*: $I_{00} = 38.6\,g\,m^{-1}$ (solid) and $15.0\,g\,m^{-1}$ (dashed); *Column b*: A350 aircraft (solid) and A320 aircraft (dashed). In the column heading, "AC" stands for "aircraft."

exceeding 100% in the N_{00}-upscaling scenarios and around 50% in the downscaling cases. However, the stronger sedimentation flux under high-shear conditions also reduces contrail-cirrus lifetime.

When varying the background relative humidity with respect to ice (c), we observe larger values of total ice mass, ice crystal number, extinction, and mean optical thickness for the higher $RH^*_{i,amb,0}$ value across all N_{00} scenarios. This can be attributed to three key factors: First, in the 110% case, fewer ice crystals survive the vortex phase. Second, the updraught-induced water vapor supply during the simulation is generally lower compared to the 120% case. Third, the initial contrail is shallower, making it less prone to horizontal spreading and subsequent ice crystal growth. In the simulation with a 100-fold reduction of N_{00} (dark blue curve), the contrail-cirrus lifetime is by around 10 min shorter in the 120% scenario, an initially counterintuitive result. In this specific case, all ice crystals survive the adiabatic heating during the vortex phase, independent of background relative humidity. The depth of the five-minute old contrail is hence the crucial factor determining the contrail-cirrus' lifetime: In the 120% case, larger ice crystals are initially present in the lower part of the contrail compared to the 110% case, leading to a stronger sedimentation flux that ultimately reduces the lifetime. This finding, however, is specific to the low-temperature case (217 K) but applies across all meteorological scenarios considered here.

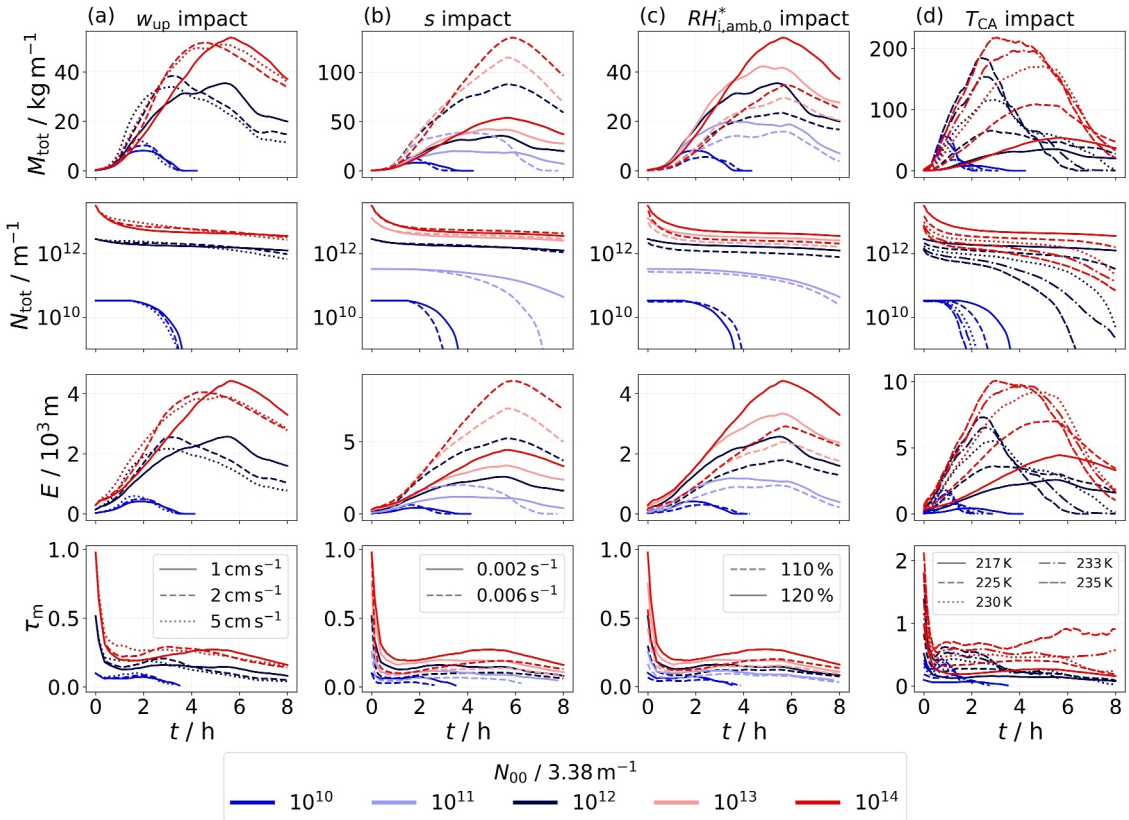

Figure 7. Temporal evolution of total ice mass, total ice crystal number, total extinction, and mean optical thickness depending on the N_{00} scaling, denoted by the colors. Baseline state: A350 aircraft with water vapor emissions characteristic of H_2 propulsion, under baseline ambient conditions listed in Table 2. *Column a*: w_{up} = 1 cm s^{-1} (solid), 2 cm s^{-1} (dashed), and 5 cm s^{-1} (dotted); *Column b*: s = 0.002 s^{-1} (solid) and 0.006 s^{-1} (dashed); *Column c*: $RH^*_{i,amb,0}$ = 110 % (dashed) and 120 % (solid); *Column d*: T_{CA} = 217 K (solid), 225 K (dashed), 230 K (dotted), 233 K (dash-dotted), and 235 K (densily dashed). In columns a and d, only the extreme scaling scenarios are displayed (factor 100 scaling) for better visibility. Note that the y-axis scales vary between columns.

The impact of ambient temperature on contrail-cirrus evolution is substantial, shown in (d). Higher ambient temperatures correspond to higher absolute humidity levels due to the exponential increase in saturation pressure, allowing more moisture to deposit onto ice crystals and promote their growth. In Figure 8, each row corresponds to a different ambient temperature, revealing a clear trend of increasing crystal size with increasing temperature. Also, simulations at higher T_{CA} already start with fewer but larger crystals, resulting from the vortex phase processes (LU25VP). Consequently, peak ice mass and total extinction are approximately between 130 and 340% ($N_{00} \sim 10^{14}$ to $N_{00} \sim 10^{10}$ m^{-1}) higher in the 235 K case compared to the 217 K scenario. The more pronounced differences in low-N_{00} contrails are further examined in Section 3.2.2. Rapid crystal growth also leads to a shorter contrail-cirrus lifetime. Ambient temperature significantly influences the evolution of the effective crystal diameter, as illustrated in Figure 9. While the increase in d_{eff} remains moderate at lower temperatures, it becomes more pronounced at higher temperatures, reaching values >100 µm in low-N_{00} contrails.

In assessing the influence of the parameters N_{00}, I_{00}, aircraft type, $RH^*_{i,amb,0}$, T_{CA}, w_{up}, and s on peak mass, extinction, and contrail-cirrus lifetime, we find that, besides N_{00}, temperature has the most significant impact on peak mass and extinction, followed by wind shear. In comparison, initial relative humidity, aircraft type, updraught speed, and initial water vapor emission are of secondary importance. However, this section offers only a partial view of the complex interdependencies involved, as the sensitivity studies presented are around a baseline state. We provide a more detailed exploration of these interdependencies in the following sections.

3.2.2. Scaling Relation Between Total Extinction and Ice Crystal Number

The study of Unterstrasser and Gierens (2010b) has related total extinction to the initial ice crystal number via the power law

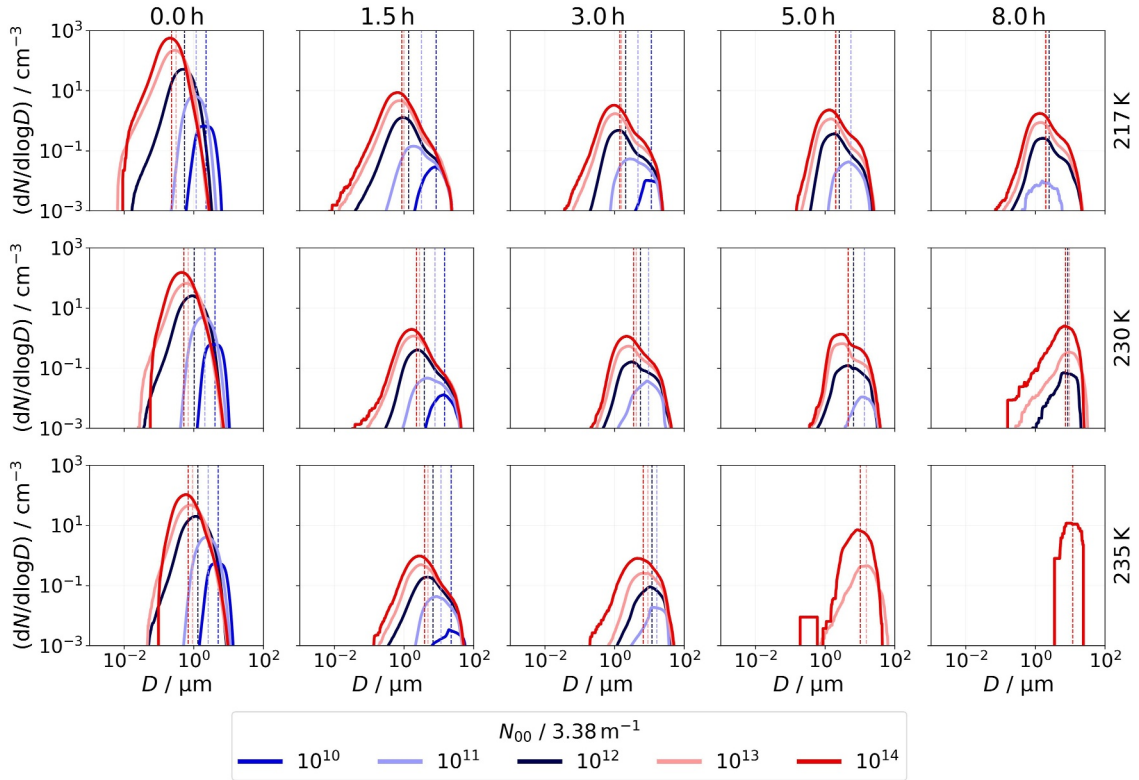

Figure 8. Temporal evolution of size spectra of ice crystal number for three ambient temperatures (rows). All other ambient conditions correspond to the baseline values (see Table 2). Time points are chosen as in Figure 3. The vertical lines indicate the mean values of the size distributions.

$$\frac{E(t)}{E_{\mathrm{ref}}(t)} = \left(\frac{N_0}{N_{0,\mathrm{ref}}}\right)^{\alpha}, \tag{10}$$

where N_0 was varied across two orders of magnitude. For the first 3 hours of contrail evolution, they found α to be approximately 0.35, capturing the instantaneous sensitivity of extinction to changes in the initial number of ice crystals. Lewellen (2014) reported a similar value of 1/3.

Extinction is related to the projected surface area A of ice crystals, which scales with $m^{\sigma/\beta}$, where m is the ice crystal mass. The constants σ and β are the exponents of empirical power law functions for area-size and mass-size relations, namely $A \sim D^{\sigma}$ and $m \sim D^{\beta}$ (Heymsfield et al., 2002; Mitchell, 1996). They depend on the ice crystal habit and size; in the simplest case, $\sigma = 2$ and $\beta = 3$ for spherical ice crystals. For crystals with non-unity

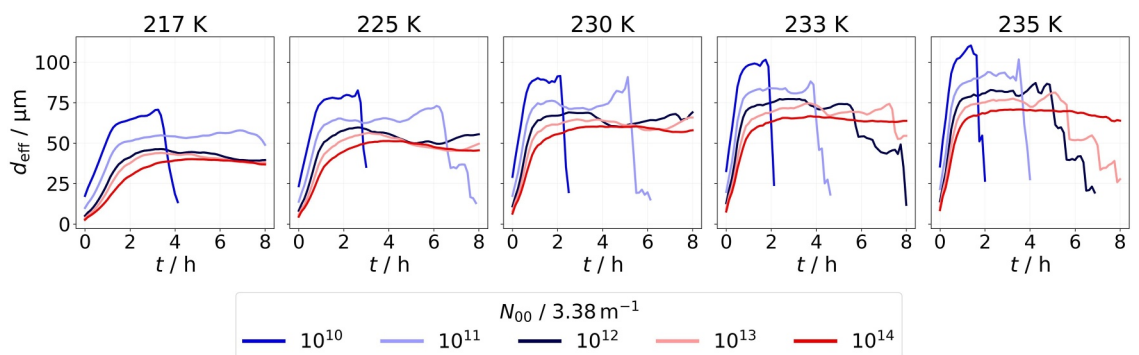

Figure 9. Evolution of effective diameter at five different values of ambient temperature. All other ambient conditions correspond to the baseline values (see Table 2).

aspect ratios, both σ and β are smaller (see Sölch & Kärcher, 2010, and references therein). Assuming a delta-function size distribution where all crystals have the same mass and size, the relation $\alpha = 1 - \sigma/\beta$ holds (see Appendix B). For spherical ice crystals, this yields $\alpha \approx 0.33$, while for hexagonal columns smaller than 100 µm, empirical relations by Mitchell et al. (1996) give $\alpha \approx 0.31$. Besides the ice crystal habit, also the shape of the size distribution affects the relation between extinction and ice crystal number. Both effects can be theoretically captured (Schumann et al., 2011). The evaluation of our model data comprises both effects. We confirm the theoretical expectations of α around 0.3 by evaluating Equation 10, which yields initial exponents $\alpha(t = t_0)$ consistently lying between 0.1 and 0.4, regardless of whether N_{00} or N_0 is used (not shown).

$\alpha(t)$ decreases across all N_{00} scaling cases during the first hour of evolution. This indicates that $E(t)$ in both upscaling and downscaling scenarios grows more slowly than in the reference case. In the upscaling cases, this can be attributed to the relatively weaker fallstreaks, the regions where most of the ice mass accumulates, thereby reducing the rate of mass growth. In the downscaling cases, the projected crystal area grows more slowly than in the reference case since the smaller ice crystal number cannot be compensated by the larger average crystal sizes. For the extreme high-temperature scenarios ($T_{CA} \geq 230$ K), $\alpha(t)$ even becomes negative in the factor-of-100 N_{00}-upscaling cases during the first 1–2 hr, due to an initially lower number of vortex phase-surviving ice crystals. Eventually, for all cases, $\alpha(t)$ diverges at later times as either $E(t)$ or $E_{ref}(t)$ approaches zero. Comparing the use of N_{00} and N_0 in the above formula, both definitions yield qualitatively similar behavior. However, the spread in initial α values around 0.3 is reduced when N_0 is used, since the range spanned by the scaling factors (i.e., 0.01, 0.1, 10, and 100) is somewhat compressed relative to those of N_{00}. As an example, the scaling factors change to 0.015, 0.14, 3.55, and 7.5 in the case of an A350 aircraft at $T_{CA} = 217$ K, $RH^*_{i,amb,0} = 120$ %, and $I_{00} = 15$ g m^{-1}.

3.2.3. Response of $\hat{E}$ to N_{00}: Contrail-Lifetime Considerations

To assess contrail significance in our study, we use the time-integrated total extinction $\hat{E}$, which is given in Equation 9. This quantity serves as a proxy for estimating the change in the climate impact of a single contrail. In our simulations, contrail-cirrus dissipation is purely microphysically driven. However, large-scale atmospheric processes, such as subsiding air masses, may create subsaturated conditions that lead to dynamically driven contrail dissipation (Bier et al., 2017; Hofer & Gierens, 2025). To approximate scenarios where synoptic-scale processes lead to faster contrail dissipation, we integrate contrail properties up to specified time limits t_{lim}, which are smaller than the total simulated time of 8 hr.

As we are interested in a relative change of contrail extinction with N_{00}, Figure 10a displays $\tilde{E}_{N_{00}} = \hat{E}(N_{00}) / \hat{E}(N_{00,ref})$ as a function of N_{00}, where color-coded $\tilde{E}(t_{lim})$ values connect vertical lines. As expected from Figures 5–7, we find an increase (decrease) in $\tilde{E}_{N_{00}}$ with increasing (decreasing) N_{00}. The temporal evolutions of total extinction, exemplarily shown in these figures, demonstrate that the peak value in the extinction evolution is eventually exceeded across all N_{00} variations at some point in time, and extinction values decrease again. Hence, the vertical distances between the symbols along a vertical line get smaller for larger t_{lim}. This effect is more pronounced when the peak extinction value is reached earlier, which occurs in the low-N_{00} regime and at high ambient temperatures. When considering contrail-cirrus evolution over a two-hour period, increasing N_{00}, especially under high-temperature conditions, has only a minor effect. The orange symbols corresponding to 110% and 120% relative humidity remain close to one, indicating little deviation from the reference extinction. This limited impact is due to substantial in situ sublimation in the upscaling scenarios during the early phase (see Section 3.2), where a large fraction of ice crystals is lost early. This is reflected in the strong early drop in ice crystal number (second row in Figures 6 and 7). Additionally, the growth in ice mass is less steep due to smaller mean crystal sizes compared to the N_{00}-reference case (Figure 8), resulting in a similar increase in early extinction $E(t < 2\,\text{h})$ between the reference and upscaling simulations. In contrast, differences between the reference and downscaling scenarios become apparent within that period. As the contrail dissipates most quickly in the scenario with a 100-fold reduction in N_{00}, the $\tilde{E}_{N_{00}}$ value is reduced to only ≈ 10 % of the reference value. Overall, we observe a greater impact of $RH^*_{i,amb,0}$ on $\tilde{E}_{N_{00}}$ in the upscaling than in the downscaling cases, particularly for long integration times.

Investigating the influence of ambient temperature on each N_{00}-scaling scenario separately, panel (b) reveals that ambient temperature plays the most significant role for short-living contrail-cirrus. Under warm conditions, that is, $T_{CA} \geq 225$ K, the ice mass gain is most pronounced in the first few hours of the contrail-cirrus lifecycle. Due to

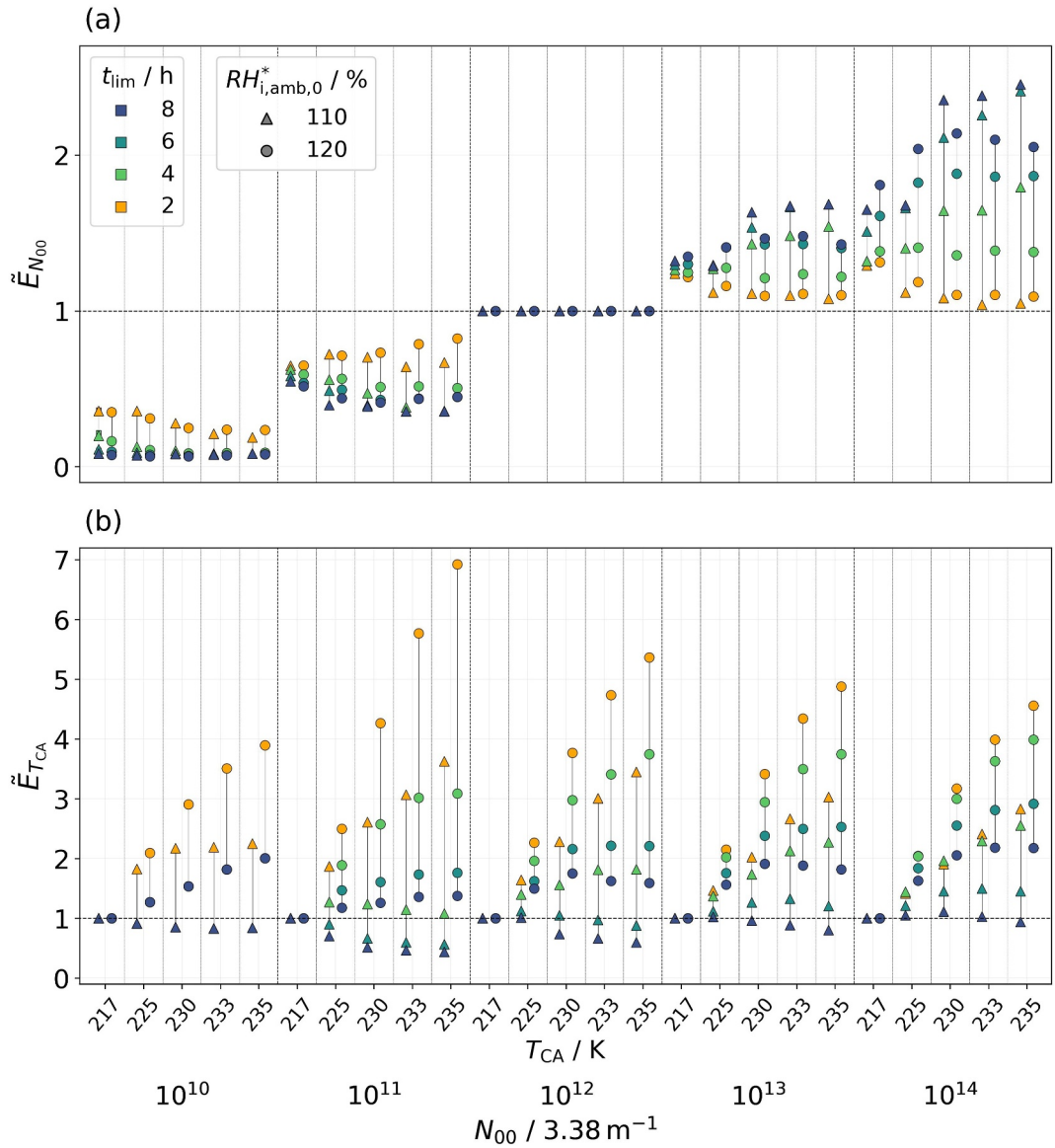

Figure 10. Normalized time-integrated total extinction $\tilde{E}_{N_{00}}$ (panel a) and $\tilde{E}_{T_{CA}}$ (panel b), that is, $\hat{E}$ normalized either by $\hat{E}(N_{00} = N_{00,ref})$ or $\hat{E}(T_{CA} = 217\,K)$. The data points represent averages over the updraught scenarios. The displayed simulations are for an A350 aircraft with $I_{00} = I_{00,H_2}$ and $s = 0.002\,s^{-1}$.

enhanced ice crystal loss because of stronger and earlier-occurring sedimentation at higher temperatures (Section 3.1), $\tilde{E}_{T_{CA}}$ gradually converges toward the 217 K reference, $\tilde{E}_{T_{CA}} = 1$, at longer integration times. In the 110 % scenarios, when T_{CA} exceeds 217 K, $\tilde{E}_{T_{CA}}$ drops below one after 6–8 hr. Although having considerably larger peak extinction values compared to the 217 K reference (e.g., at 235 K and $N_{00} \sim 10^{11}\,m^{-1}$ the peak is roughly a factor of seven higher), high-T_{CA} contrail-cirrus dissipate quickly, leading to a relatively lower lifetime-integrated total extinction. Examining the temporal evolutions of total extinction, peak total extinctions increase more strongly with higher T_{CA} values in the 120% scenarios compared to the 110% humidity cases (not shown). This contrast is due to the lower availability of ambient water vapor in the 110% scenarios, limiting the growth of the ice crystals. For this reason, the temperature impact is generally more significant for 120% than for 110% relative humidity across all N_{00} simulations (circles deviate stronger than triangles from the reference). Additionally, the spread in high-temperature cases is particularly large in the $N_{00} \sim 10^{11}\,m^{-1}$ scenario but becomes smaller in the $N_{00} \sim 10^{10}\,m^{-1}$ case, where the very low number of ice crystals cannot be compensated by

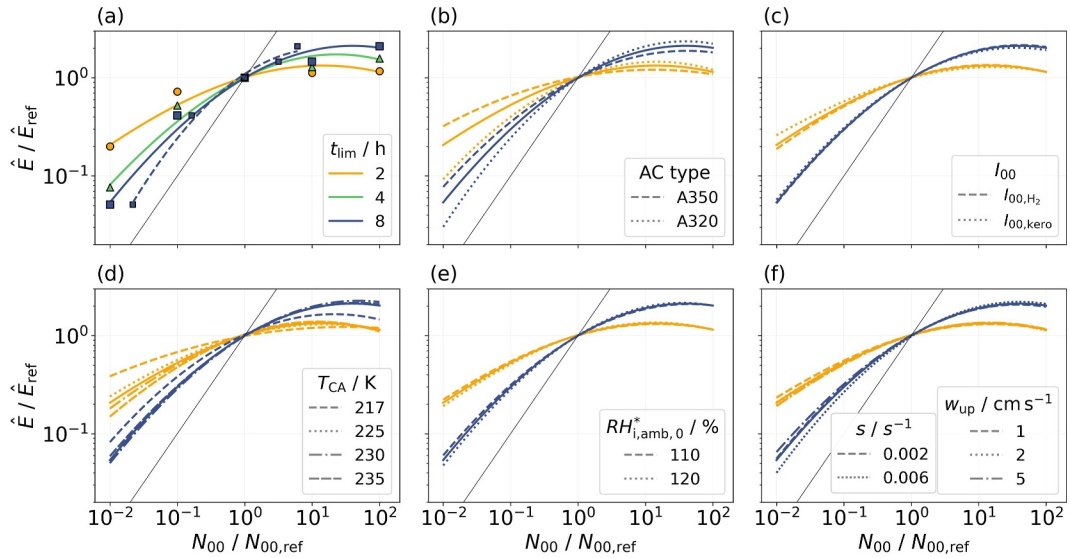

Figure 11. Normalized time-integrated total extinction as a function of the normalized initial number of ice crystals. Gray lines depict one-to-one lines. (a) Average values over aircraft type, I_{00}, T_{CA}, $RH^*_{i,amb,0}$, w_{up}, and s for time integration limits of 2, 4, and 8 hr. For $t_{lim} = 8$ h, the dashed line connecting smaller symbols indicates that $N_0/N_{0,ref}$ is used as x-axis. The orange and blue solid lines displayed in panel (a) are also shown in panels (b) to (f). (b) Sensitivity to aircraft type. (c) Sensitivity to I_{00}. (d) Sensitivity to T_{CA}. (e) Sensitivity to $RH^*_{i,amb,0}$. (f) Sensitivity to w_{up} and s (the dashed lines of $w_{up} = 1$ cm s^{-1} and $s = 0.002$ s^{-1} are identical). Note that only $t_{lim} = 2$ h and $t_{lim} = 8$ h curves are displayed in panels (b) to (f) to better differentiate between curves with different line styles. Data points are shown in panel (a), while panels (b) to (f) present fitting curves only. In panel (f), the dashed and dotted lines that can be differentiated from the mean state refer to the s-variation as the w_{up}-lines closely align with the solid lines.

temperature-induced crystal growth. This finding is independent of relative humidity. Overall, the trend of the $\tilde{E}_{T_{CA}}(t_{lim} = 8\,h)$ values (blue) remains approximately constant (at 120%) or even decreases (at 110%) with increasing temperature $T_{CA} \geq 230$ K, except the factor-of-100 N_{00}-downscaling, 120% humidity case. Therefore, we do not expect a substantial increase in total extinction compared to the 217 K reference when temperature is increased further within one N_{00}-scaling setup.

In summary, raising N_{00} barely changes contrail-cirrus extinction during the first 2 hr because the majority of the ice crystals sublimate in that period (see Figure 4). By contrast, reducing N_{00} leads to a significant effect already within that phase, as the low-N_{00} contrails dissipate before the 4 hr mark under conditions of low humidity and high temperature. At high temperatures ($T_{CA} \geq 225$ K), contrail-cirrus initially gain ice mass rapidly, leading to large peak extinction values early (i.e., within 2 hr). However, strong sedimentation causes them to dissipate quickly, so their integrated extinction approaches or even falls below the 217 K reference after 6–8 hr. We provide implications of these findings in Section 5.

3.2.4. Impact of N_{00} Scaling on Mean Normalized $\hat{E}$ Across Parameter Variations

In the following, we show the average of $\hat{E}$ across all ambient and meteorological conditions, aircraft type, and water vapor emission values considered in this study. The resulting normalized values are shown in Figure 11a. The fitting curves exhibit nonlinear behavior: While upscaling N_{00} by a factor of 100 leads only to a factor of 1.2 in $\hat{E}/\hat{E}_{ref}$ for $t_{lim} = 2$ h, downscaling by a factor of 100 results in a fivefold difference. Increasing the integration time generally leads to a steepening of the curves, particularly in the low-N_{00} regime, where the contrail-cirrus dissipates within a few hours (see Section 3.2). As a result, the reduction in $\hat{E}$ relative to the reference becomes more pronounced for longer-living contrail-cirrus, increasing from a factor of 5 to a factor of 20. At the high-N_{00} end, however, the increase in $\hat{E}$ compared to the reference is much smaller than in the low-N_{00} regime, with $\hat{E}/\hat{E}_{ref}$ increasing only from a factor of 1.2 to a factor of 2.1. Further, we show $\hat{E}/\hat{E}_{ref}$ as a function of $N_0/N_{0,ref}$ (accounting for ice crystal number reduction during vortex phase), displayed as dashed line. This curve

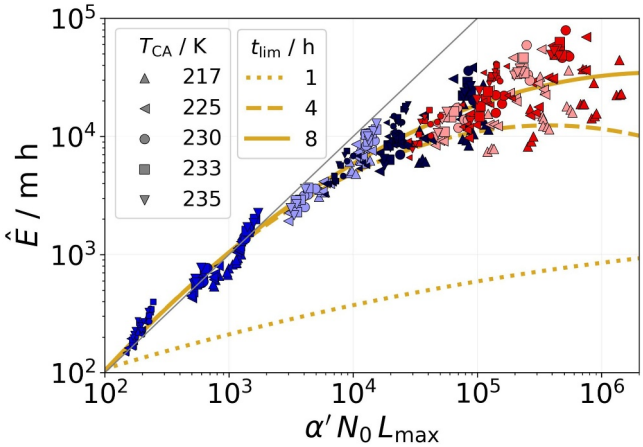

Figure 12. Extinction scaling based on Equation 5 in Lewellen (2014). Colors as in Figures 3 and 5–9. Symbols indicate ambient temperature, whereas symbol size represents the aircraft type (small symbols for A320 aircraft). No differentiation is made between different values of I_{00}, $RH^*_{i,amb,0}$, w_{up}, and s. The gray line represents the one-to-one relationship, and the orange solid line shows the best-fit curve to the data points. The dotted and dashed orange lines correspond to fits of data points when integrating only up to 1 and 4 hr, respectively (these data points are not shown in the plot). α' is defined analogously to its definition in L2014, $\alpha' = 18\pi\frac{\mu}{g\rho_i}$ with μ as air viscosity, g as gravitational constant, and ρ_i as ice density.

is closer to the one-to-one line as relatively more ice crystals are present in the N_{00}-downscaling cases compared to the upscaling cases.

Panels (b) to (f) display the average curves for integration times of 2 and 8 hr (i.e., short- and long-living contrail-cirrus), with each panel illustrating the effect of a specific parameter variation around the mean state. Focusing on a reduction in the initial ice crystal number, $N_{00}/N_{00,ref} < 1$, contrail extinction decreases relative to $\hat{E}_{ref}$ in scenarios involving a smaller aircraft with increased water vapor emission, higher ambient temperatures, and under conditions of high supersaturation. This indicates that, when few but large ice crystals are present after the vortex phase, a humid environment with ample available water vapor promotes rapid sedimentation. The opposite, that is, higher $\hat{E}/\hat{E}_{ref}$ values, is observed for the N_{00}-uscaling, yet the effect is less pronounced. Overall, we find the largest deviations from the mean state for variations in aircraft type and ambient temperature, particularly for short integration times, as anticipated in Section 3.2. Overall, a reduction in the initial ice crystal number by factors of 100 and 10 decreases mean total extinction by factors of approximately 20 and 2, respectively. Conversely, increasing N_{00} by factors of 10 and 100 leads to an increase in total extinction by factors of approximately 1 and 2, respectively. The most significant reduction is observed for an A320 aircraft, where a factor 100 decrease in N_{00} results in a factor 33 reduction in mean total extinction.

4. Model Intercomparison

In the following, we compare our EULAG-LCM results with those of a LES study (Section 4.1) and with results of the Contrail Cirrus Prediction model (CoCiP) and the Global Circulation Model (GCM) ECHAM5-CCMod (Section 4.2).

4.1. Comparison to LES Study

One of the most comprehensive study on contrail-cirrus simulations has been performed by Lewellen (2014), which comprises more than 200 large-eddy simulations using a binned microphysics scheme over a broad range of parameter variations. Lewellen (2014), hereafter L2014, derived simplified formulations that relate the contrail's maximum and lifetime-integrated properties to simulation input parameters and contrail properties determined from the simulation data. The scaling properties derived from L2014's simulation data can serve as a means to compare the simulation results of different contrail-cirrus models. A direct comparison of simulation results is often hampered by the fact that different modeling studies use different baseline conditions, and comparisons of results with slightly differing setup parameters remain inconclusive. Applying the relations proposed in L2014 to our data set allows us to evaluate whether EULAG-LCM and the model used in L2014 predict consistent trends for key contrail properties, such as maximum total ice mass, contrail width, and total extinction. The latter is half the projected ice crystal surface area as used in L2014. These quantities depend not only on prescribed parameters (e.g., cruise-altitude temperature, ambient humidity, wind shear) but also on simulation-derived variables, such as maximum contrail depth and lifetime. Hence, the simplified model cannot be used to predict contrail-cirrus properties simply from given environmental and initial contrail properties. The strength of the simplified model is to relate various properties of the simulated contrail using simple relationships.

We first consider the relation between the lifetime-integrated surface area of the ice crystals to the number of ice crystals surviving the vortex phase and the maximum contrail depth during contrail-cirrus evolution: $\hat{S} \sim \alpha' N_0 L_{max}$ (Equation 5 in L2014). Replacing $\hat{S}$ with $\hat{E}$, Figure 12 illustrates whether our simulation data support this scaling relation. Our results exhibit the same linear trend predicted by the model, with a strong clustering of data points regarding N_{00} sensitivity, represented by color. Slight deviations from this linear relationship occur only in high-N_{00} and low-temperature simulations. Section 5 provides a detailed discussion of this

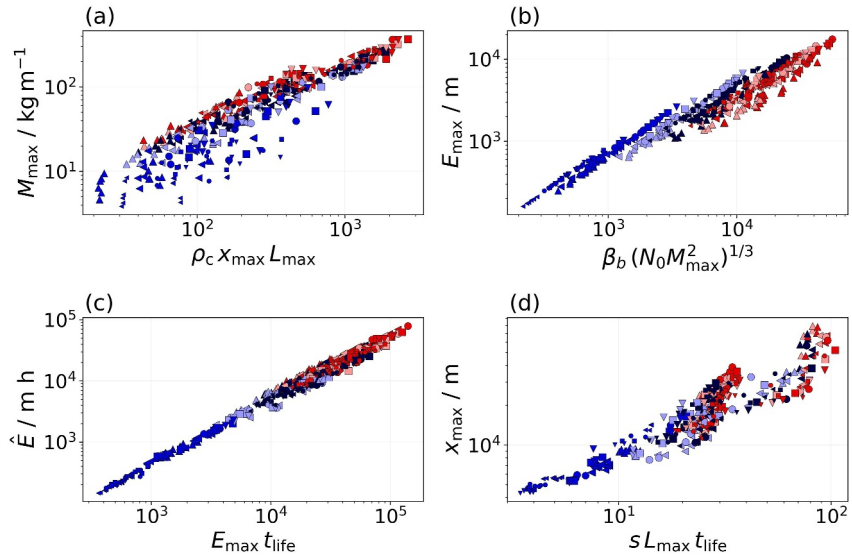

Figure 13. Scaling relations as given in Equation 11a–11d. According to L2014, $\beta_b = \left(36\pi/\rho_i^2\right)^{1/3}$. Colors, symbols, and symbol sizes as in Figure 12.

finding. Fitting curves to the data are displayed by the orange lines, where the data points only of the $t_{lim} = 8\,h$ scenario are shown.

Furthermore, L2014 provides scaling relations for maximum ice mass M_{max}, maximum surface area (in our case maximum total extinction E_{max}), time-integrated surface area (in our case time-integrated total extinction $\hat{E}$), and maximum contrail width x_{max}:

$$M_{max} \sim c_a \rho_c x_{max} L_{max} \tag{11a}$$

$$E_{max} \sim c_b \beta_b \left(N_0 M_{max}^2\right)^{1/3} \tag{11b}$$

$$\hat{E} \sim c_c E_{max} t_{life} \tag{11c}$$

$$x_{max} \sim c_d s L_{max} t_{life} \tag{11d}$$

We apply these to our results for cross-validation, as shown in Figure 13. As noted by L2014, the maximum ice mass is related to the available water vapor in the atmosphere ρ_c, calculated by $\rho\, q_{sat}(RH^*_{i,amb,0} - 1)$, initially and at cruise altitude, multiplied by the contrail-cirrus cross-sectional area $x_{max} L_{max}$ (panel a). The maximum ice crystal surface area or extinction can be estimated using $\left(N_0 M_{max}^2\right)^{(1/3)}$ (panel b). The integrated total extinction is simply the product of the maximum total extinction and the contrail lifetime t_{life} (panel c). Additionally, the maximum contrail width is related to shear, multiplied by the maximum contrail depth and lifetime (panel d). By fitting lines to our data points, we obtain slopes of $c_a = 0.14, c_b = 0.29, c_c = 0.52$, and $c_d = 0.15$, which we compare to the values reported in L2014: $c_{a,L2014} = 0.08, c_{b,L2014} = 0.7, c_{c,L2014} = 0.56$, and $c_{d,L2014} = 0.25$. The difference in c_b can be attributed to our use of total extinction, which is approximately half of the total surface area used in L2014. Consistent with the findings in L2014, we observe a steeper slope in panel (b) for low-N_{00} scenarios. Differences in c_a and c_d between L2014 and our study may arise from differing definitions of contrail width. As the contrail-cirrus evolves, no distinct spatial boundaries can be defined. Hence, thresholds based on individual judgment must be applied, which may explain variations in the derived x_{max} values. In our approach, we determine the contrail width by including all columns containing a nonzero number of ice crystals. These are first stored in binary format and then smoothed. By applying a threshold to the smoothed data of 0.05, we identify which columns are included in the width calculation. This allows us to account for diffused regions of the contrail-cirrus that are loosely connected to the bulk, while excluding isolated patches that are completely detached.

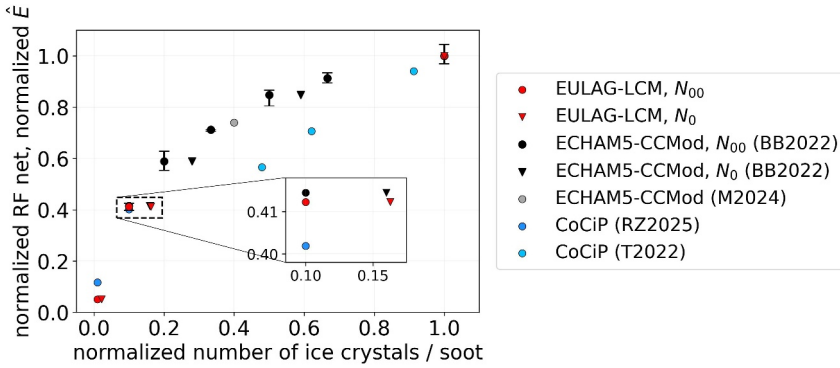

Figure 14. Mean normalized net radiative forcing, computed using ECHAM5-CCMod (Bier and Burkhardt (2022) (black), Märkl et al. (2024) (gray)), and CoCiP (Rubin-Zuzic et al. (2025) (blue), Teoh et al. (2022) (light blue)), presented alongside the mean normalized time-integrated total extinction values from our study (red). Data points from ECHAM5-CCMod and CoCiP are plotted against the normalized soot emission (circles), while data points from Bier and Burkhardt (2022) and our study are additionally plotted against the normalized number of ice crystals surviving the vortex phase (triangles).

4.2. Comparison to CoCiP and GCM Studies

Section 4.1 dealt with the comparison of high-resolution contrail-cirrus simulations from two different LES codes. In a next step, we compare our results with two further contrail models that operate on different spatial and temporal scales, namely CoCiP (Schumann, 2012) and the GCM ECHAM5-CCMod (Bock & Burkhardt, 2016; Burkhardt & Kärcher, 2011). Both models have been used in the past to examine the sensitivity of contrail-cirrus properties to a variation of ice crystal number (Bier & Burkhardt, 2022; Burkhardt et al., 2018; Rubin-Zuzic et al., 2025; Teoh et al., 2022). While it is tempting to compare the outcomes of the three modeling approaches, such comparisons must be made with caution due to significant differences in spatial scales and mesh resolutions, which in turn influence the relevance, selection, and implementation of physical processes. These include, for example, saturation effects in contrail clusters, cloud overlap, interactions with natural clouds, and the representation of early contrail formation processes during initialization. Furthermore, the studies differ in their choice of reference ice crystal numbers and base years. In the case of EULAG-LCM, no specific base year is defined as we provide an unweighted mean over all considered simulation setups (see Table A1). Bier and Burkhardt (2022) (hereafter, BB2022), Märkl et al. (2024) (hereafter, M2024), Teoh et al. (2022) (hereafter, T2022), and Rubin-Zuzic et al. (2025) (hereafter, RZ2025) evaluate the impact of contrail ice crystal number on the net radiative forcing (RF), whereas the present study evaluates the time-integrated total extinction. Radiative transfer calculations as in Forster et al. (2012) suggest a linear relationship between $\hat{E}$ and instantaneous RF for fixed irradiances, that is, contrail properties change while the radiative scenario is unchanged, such that the radiative fluxes impinging the contrail layer remain the same (not shown).

Using the ECHAM5-CCMod model over five simulated years, BB2022 estimate the change in global mean net RF due to contrail-cirrus resulting from a reduction in soot number emissions. Their study reduces the reference soot number emissions by 90%, 80%, 67%, 50%, and 33%, as represented by the black circles in Figure 14. For the 90% reduction case, this leads to a 59% decrease in mean RF compared to the reference scenario. The study of M2024 applies ECHAM5-CCMod to estimate the reduction of contrail-cirrus RF for a 60% reduction in soot number concentration. They found a reduction of 26% in RF for a global fleet using 100% SAF in the year 2018. The corresponding data point agrees with previous ECHAM5-CCMod studies and is shown in gray in Figure 14.

Similarly, using CoCiP for the European region in the year 2019, RZ2025 reports a 60% and 88% reduction in mean normalized net RF when soot emissions are decreased by 90% and 99%, respectively. These data points are shown in blue in Figure 14. For the 90% reduction case, our work aligns with both studies, BB2022 and RZ2025, as we find a 59% reduction in mean $\hat{E}$. For the 99% reduction case, we find the larger reduction in mean $\hat{E}$ of 95% compared to the value of 88% suggested by CoCiP. Also using CoCiP, T2022 investigated the use of SAF blends on the contrail climate impact in the North Atlantic for 2019. Data points corresponding to 10%, 50%, and 100% SAF blending ratios are shown in light blue. Generally, their mean net RF appears lower than with the GCM, indicating a stronger impact of reducing the initial particle number on the contrail-cirrus radiative effect. The deviation from GCM results, as well as potential discrepancies with the CoCiP study by RZ2025 when

Table 3
Comparison of Modeling Approaches Regarding Contrail Properties[a] and Effect of Soot or N_{00} Reduction on Contrail-Cirrus Radiative Properties[b,c]

	c_a	c_b	c_c	c_d	Norm. $\hat{E}$ or RF net 90% red. in soot/N_{00}	Norm. $\hat{E}$ or RF net 99% red. in soot/N_{00}
EULAG-LCM	0.14	0.29	0.52	0.15	0.41	0.05
Comparison studies	0.08[a]	0.7[a]	0.56[a]	0.25[a]	0.41[b], 0.40[c]	0.12[c]

[a]Lewellen (2014): Fitting coefficients for scaling relations of contrail properties, given in Equations 11a–11d. [b]Bier and Burkhardt (2022): global average of RF net over 5 years. [c]Rubin-Zuzic et al. (2025): average of RF net across the European region for the year 2019.

extrapolating to lower initial particle numbers, indicates that the RF sensitivity to ice crystal number in CoCiP (or possibly also in other models) depends also on the specific model application.

BB2022 accounts for ice crystal loss during the vortex phase by implementing the vortex phase parameterization of Unterstrasser (2016). Consequently, Figure 14 also presents results as a function of the normalized number of ice crystals surviving the vortex phase, represented by triangles for both ECHAM5-CCMod and our study. In both cases, a 84 % reduction in ice crystal number is observed when the nucleated number of ice crystals is reduced by 90 %. This agreement is expected, as both models account for vortex-phase losses similarly, ECHAM5-CCMod through the parametrization and our study via the prescribed initial conditions.

Overall, the three models find fairly similar reduction rates for the 90% and 99% cases. Given that contrail-cirrus are simulated on different spatial scales, true reduction rates can differ and may, in reality, depend on the considered spatial scales. Hence, the partly excellent agreement should not obscure the fact that we cannot expect the true outcomes for the considered scenarios with the various models to match. Nevertheless, the consistency in the trends strengthens confidence in the robustness and plausibility of the simulation results. Table 3 provides a summary of our comparison study.

In our results sections, we describe changes relative to the reference in terms of multiplicative factors, whereas the above comparison uses additive (percentage) changes. Both approaches have their justifications, but the additive one can obscure the strong non-linearity between ice crystal number and $\hat{E}$ or RF. For instance, reducing the ice crystal number by 99 % lowers $\hat{E}$ by 95 %. At first glance, this might suggest changes of similar magnitude. However, a 100-fold decrease in ice crystal number reduces $\hat{E}$ by only a factor of 20.

5. Discussion

This study aims to provide an overview of the potential implications of alternative aircraft propulsion on the contrail radiative effect. A hypothetical SAF- or H_2-propulsion setup is represented by systematically increasing and decreasing the number of initially nucleated contrail ice crystals in the model. Also, the initially emitted water vapor by the aircraft engines is adapted, although we find its influence on the later contrail-cirrus properties to be minor.

We want to emphasize the importance of differentiating between synoptically controlled versus sedimentation-dominated regimes: The influence of alternative fuels is weaker on short-living contrail-cirrus in a synoptically controlled regime than on long-living contrail-cirrus in sedimentation-dominated regimes, as already found in a global modeling study (Bier et al., 2017). The effect of SAF or H_2 as a combustion fuel becomes exceptionally significant after few hours when the low-N_{00} contrail-cirrus has dissipated compared to a long-living kerosene contrail. While H_2 contrails form more frequently than kerosene contrails (Hofer et al., 2024), their comparatively short lifetimes tend to counteract this effect. Also, the impact of ambient temperature on contrail-cirrus evolution is more pronounced in synoptically controlled regimes characterized by subsidence, where rapid ice mass growth leads to considerably higher extinction values (Figure 10b). Under warm conditions, contrail-cirrus typically consists of fewer but larger ice crystals, whereas colder conditions favor smaller crystals. In regimes characterized by subsidence, both contrail types dissipate more quickly compared to sedimentation-dominated scenarios. However, due to faster ice crystal growth and higher extinction values, contrails formed in a warm atmosphere can contribute more strongly to radiative forcing before dissipating. In contrast, in sedimentation-driven regimes, the radiative impact differs. While warm-case contrail-cirrus experience rapid growth, they also exhibit shorter lifetimes due to the efficient sedimentation of large ice crystals. Conversely, cold-case contrail-cirrus develop more slowly but persist significantly longer, as smaller ice crystals sediment

more slowly. As a result, despite lower peak extinction, contrails in cold conditions can exert a larger radiative impact over time. This finding is particularly relevant for H_2 combustion, which is expected to produce contrail-cirrus with fewer but larger ice crystals.

In our simulations, we neglect several physical processes, such as the formation of natural cirrus by homogeneous or heterogeneous nucleation, the radiative heating of the contrail, and ice crystal aggregation. The evolution of an individual contrail can be perturbed by surrounding natural cirrus, as the study by Unterstrasser, Gierens, Sölch, and Wirth (2017) has shown. The presence of natural cirrus below the contrail hampers the development of fallstreaks, potentially prolonging contrail lifetimes, which could be especially relevant in the N_{00}-downscaling simulations. Additionally, in order to maintain clarity and isolate the effects of H_2 propulsion on contrail properties, we chose to simulate individual contrails rather than contrail clusters, thereby avoiding added complexity in interpreting our results.

Furthermore, radiation alters the contrail-cirrus evolution as shown by past studies (Lewellen et al., 2014; Unterstrasser & Gierens, 2010b). Solar and thermal radiation entering the contrail layer interact with the ice crystals, changing the internal contrail dynamics. During a cloudless summer day, this leads to an updraft motion, and the temperature within the contrail decreases adiabatically, thereby increasing the relative humidity in the contrail (Unterstrasser & Gierens, 2010b). The increasing ice mass then leads to a higher total extinction. We suspect that in case of a high-N_{00} contrail, radiation and an imposed updraft motion could prevent some of the small ice crystals from sublimating in situ as the radiation impact becomes considerable already within the first 3 hr, where most of the sublimation in the N_{00}-upscaling scenarios happen (Figure 4). In contrast, the low-N_{00} contrails might experience even stronger sedimentation in radiation-driven updraft situations. The already large ice crystals would grow even larger and fall out more rapidly, lowering the contrail-cirrus lifetime. This implies that the differences between high- and low-N_{00} contrails could be amplified once radiative effects are considered, with higher extinction values and longer-living contrails in the former and shorter-living contrails in the latter case. Then, the curves in Figure 11 potentially exhibit larger slopes. Despite these expectations, we have chosen to model contrail-cirrus in a setup without radiation to avoid introducing additional complexity that would make it difficult to disentangle the underlying processes.

The study of Gierens (2012) showed that aggregation plays a role in contrail-cirrus embedded in naturally formed cirrus clouds. In such cases, sedimenting ice crystals from the natural cirrus layer may interact with the contrail below, depleting contrail ice mass through aggregation. However, as our setup does not include natural cirrus formation or interactions, this process is not considered here. Nevertheless, since sedimentation velocities in low-N_{00} contrails can be comparable to those in natural cirrus, neglecting aggregation between contrail ice crystals might introduce a bias in these cases. This is particularly important for the fallstreak regions, where sedimentation is strongest and large crystals dominate (see Figure 3). However, as aggregation effects scale with the square of ice crystal number concentration (Gierens, 2012; Unterstrasser, Hoffmann, & Lerch, 2017), the low number concentrations in the fallstreaks are expected to compensate for the high sedimentation velocities there, potentially limiting the significance of aggregation in low-N_{00} contrails. Additionally, the narrow size distribution of ice crystals in the fallstreaks (Figure 11 in Unterstrasser, Gierens, Sölch, and Lainer (2017)) suggests only minor differences in sedimentation velocities, further reducing the expected influence of aggregation.

Lastly, we discuss the implications of our chosen vertical relative humidity profile. Initially, the thickness of the ISSL is either 1,100 or 1,180 m depending on the prescribed humidity value at flight altitude. The flight level, set at $z = 2{,}000$ m in the simulation domain, is located at the top of the ISSL (Figure 1a). Altering the setup by lowering the flight altitude to $z = 1{,}500$ m or by reducing the ISSL's thickness to 500–600 m would likely lead to a different evolution of contrail total extinction. The relative contribution of fallstreak ice crystals to total extinction increases over time (Figure 3). A thinner ISSL reduces the vertical extent of fallstreaks, which in turn lowers extinction values and accelerates contrail dissipation. While high-N_{00} contrails would be largely unaffected, since core ice crystals dominate their extinction, this sensitivity is particularly relevant for low-N_{00} contrails, where nearly all ice mass resides in the fallstreaks. Hence, the extinction and lifetime estimates for low-N_{00} contrails in our current configuration may represent upper bounds, assuming the ISSL is on average thinner.

The comparison with the study by L2014 shows good agreement, with our results confirming the proposed scaling relations based on the slopes obtained from linear fits. One notable discrepancy between L2014 and our study appears in Figure 12, which shows the relationship between $\hat{E}$ and $N_0 L_{\max}$. While L2014 reports an excellent

linear relationship, our data exhibit a deviation from linearity in the high-$\hat{E}$ regime. One may argue that extending the simulation period would improve the alignment of our data points with the one-to-one line in that regime. This interpretation is supported by our observation that the fitted curves converge toward the one-to-one line as the time-integration limit increases, as illustrated by the orange fitting lines in Figure 12. For a small time limit of 1 hr, the slope of $\hat{E}(\alpha' N_0 L_{\max})$ is much smaller than one. We repeated a set of 32 simulations, where we extended the simulation period from 8 to 20 hr. As expected, the resulting data points move closer to the one-to-one line, but a noticeable gap remains (not shown). This occurs because the total extinction often starts to decline once the updraught ceases (Figure 5). Hence, extending the integration limit does increase $\hat{E}$, but the data points are still far from the one-to-one line. We consider this deviation reasonable, as in real-world conditions, the lifetime of ice supersaturated regions in the atmosphere typically does not exceed a few hours (Irvine et al., 2014), and large-scale subsidence often leads to subsaturation and contrail dissipation. Therefore, updraughts lasting up to 12 hr and producing ice supersaturations as high as 1,800 %, as in the simulations of L2014 (where natural cirrus formation in the contrail vicinity was not accounted for), should be considered highly idealized. Hence, we deem a less-than-linear relationship between the time-integrated total extinction and the initial ice crystal number more reasonable.

In Figure 11, we expect that further increasing N_{00} would not significantly increase the normalized time-integrated total extinction, even for long integration times. This is due to three reasons. First, higher N_{00} values result in lower ice crystal survival fractions during the vortex phase, yielding N_0 values comparable or even smaller to those already considered. Second, the resulting smaller core ice crystals would be even more prone to in situ sublimation than in the cases studied so far. Third, peak extinction, which is roughly timed with the termination of updraught motion, occurs within 8 hr in our simulations, and this point in time is independent of N_{00} if $N_{00} \geq 10^{12}\,\mathrm{m}^{-1}$ (Figure 5d). As a result, further increases in N_{00} would likely yield similar total extinction evolutions. At the low-N_{00} end, further reducing N_{00} is unlikely to affect vortex-phase survival fractions, at least in high-humidity cases, since the number of surviving ice crystals there is already one or close to one. However, these very few but large ice crystals would sediment more rapidly during the dispersion phase, leading to a shorter contrail-cirrus lifetime. Overall, we expect that the general nonlinear shape of the curves in Figure 11 would remain largely unchanged, even with more extreme variations in N_{00}.

6. Conclusion

Using the LES code EULAG coupled to the particle-based cloud module LCM, we simulated contrail-cirrus behind SAF- or H_2-powered aircraft. Building on a previous study that examined H_2 contrails in the first few minutes after formation, we use those simulations as initial conditions. These contrails are characterized by a broad range of nucleated ice crystal numbers N_{00}, spanning from 10^{10} up to 10^{14} ice crystals per flight meter, and larger ice crystal sizes due to the increased water vapor emission. We conducted 400 contrail-cirrus simulations, accounting for variations in ambient relative humidity with respect to ice, ambient temperature, updraught-induced adiabatic cooling, and vertical wind shear. Simulations for an A350/B777-like aircraft and a smaller A320/B737-like aircraft have been performed. While we have chosen the larger aircraft for compatibility with previous studies (Unterstrasser, Gierens, Sölch, & Lainer, 2017; Unterstrasser, Gierens, Sölch, & Wirth, 2017), the smaller aircraft better mimics the design concepts of future hydrogen aircraft. Our results indicate that in situ sublimation is the main driver for ice crystal loss in high-N_{00} contrails, whereas low-N_{00} contrail-cirrus exhibit stronger sedimentation fluxes, leading to faster dissipation. In general, we find a nonlinear dependency of time-integrated total extinction $\hat{E}$ to N_{00}. The impact of ambient temperature, especially in cases where ambient temperature exceeds 230 K, is most pronounced for short-lived contrail-cirrus. We find a stronger overall reduction in $\hat{E}$ for the smaller of the two studied aircraft types. Averaging across all ambient conditions, we find that a 100-fold reduction in N_{00} leads to a 20-fold reduction in $\hat{E}$. In percentage terms, this is equivalent to a 95% reduction in $\hat{E}$ for a 99% reduction in N_{00}. Similarly, a 10-fold reduction in N_{00} results in a 2-fold decrease in $\hat{E}$, corresponding to a 59% reduction in $\hat{E}$ for a 90% reduction in N_{00}. Our study is consistent with previously established scaling relations for contrail ice mass, width, and total extinction. Furthermore, comparisons with results from ECHAM5-CCMod and CoCiP show good agreement, demonstrating a similar contrail response to a soot/ice crystal number variation despite analyzing the effect on different spatial scales and considered time periods. The interaction of H_2 contrail-cirrus with natural cirrus and the roles of radiation and aggregation in the H_2 contrail-cirrus evolution are the foci of future work.

Appendix A: Initial Contrail-Cirrus Properties

Table A1 provides an overview of the vortex phase simulations presented in Lottermoser and Unterstrasser (2025), which serve as initial conditions for the contrail-cirrus simulations of the present study.

Table A1
Properties of the Initialized Contrails[a]

Aircraft type	T_{CA}/K	$RH_{i,amb}$/%	$I_{00}/(\mathrm{g\,m^{-1}})$	$N_0/(10^{12}\,\mathrm{m^{-1}})$	$I_0/(\mathrm{g\,m^{-1}})$
A350/B777	217	110	15.0	0.02, 0.15, 0.95, 3.34, 6.93	4.7, 7.1, 7.5, 7.0, 6.2
			38.6	0.03, 0.27, 2.13, 9.25, 22.08	7.8, 12.0, 13.7, 14.0, 13.2
		120	15.0	0.03, 0.3, 2.18, 7.74, 16.36	12.7, 19.6, 21.4, 21.9, 20.8
			38.6	0.03, 0.33, 2.85, 13.14, 31.84	15.0, 22.3, 24.5, 24.4, 23.7
	225	110	15.0	0.02, 0.08, 0.43, 1.19, 2.19	9.7, 11.5, 11.3, 10.2, 9.1
			38.6	0.02, 0.16, 0.98, 3.25, 6.8	14.8, 21.3, 23.7, 21.6, 19.5
		120	15.0	0.03, 0.26, 1.51, 4.21, 8.2	34.0, 50.9, 53.2, 50.3, 45.5
			38.6	0.03, 0.3, 2.12, 7.1, 15.03	37.5, 55.4, 59.1, 59.0, 54.6
	230	110	38.6	0.02, 0.11, 0.59, 1.71, 3.35	24.6, 31.0, 29.8, 26.1, 23.2
		120	38.6	0.03, 0.28, 1.73, 4.91, 9.94	74.7, 105.2, 112.3, 106.8, 98.5
	233	110	38.6	0.02, 0.09, 0.46, 1.25, 2.37	31.3, 37.5, 35.8, 31.6, 28.2
		120	38.6	0.03, 0.26, 1.52, 4.14, 8.17	107.0, 149.6, 159.9, 151.3, 138.1
	235	110	38.6	0.01, 0.08, 0.4, 1.04, 1.92	37.3, 43.8, 41.9, 36.9, 32.7
		120	38.6	0.03, 0.25, 1.45, 3.75, 7.41	136.7, 189.0, 200.5, 189.8, 174.0
A320/B737	225	110	3.7	0.01, 0.25, 1.13	5.0, 9.5, 6.9
			9.5	0.01, 0.44, 2.97	5.9, 12.5, 11.5
		120	3.7	0.01, 0.66, 3.86	13.3, 25.8, 23.2
			9.5	0.01, 0.72, 5.71	14.0, 27.0, 24.9
	230	110	9.5	0.01, 0.3, 1.55	8.6, 18.1, 15.5
		120	9.5	0.01, 0.68, 4.19	23.2, 44.5, 42.2
	233	110	9.5	0.01, 0.25, 1.2	12.3, 24.3, 19.2
		120	9.5	0.01, 0.66, 3.78	33.6, 64.6, 60.6
	235	110	9.5	0.01, 0.23, 1.04	15.6, 29.8, 22.6
		120	9.5	0.01, 0.65, 3.46	43.4, 81.0, 76.7

[a]Total ice crystal number N_0 and mass I_0 after vortex phase as functions of the respective aircraft, ambient temperature, ambient relative humidity with respect to ice, and initial amount of emitted water vapor according to Table 1. For the A350/B777-like aircraft, five values are provided for N_0 and I_0, which denote the N_{00}-scaling simulations with scaling factors 0.01, 0.1, 1, 10, and 100. For the smaller A320/B737-like aircraft, N_0 and I_0 values are available for scalings of 0.01, 1, and 100.

Appendix B: Derivation of α in Extinction Scaling

We consider two ice crystal populations: one with $N_{p,1}$ identical ice crystals of mass m_1 and size D_1, and the other with $N_{p,2}$ identical ice crystals of mass m_2 and size D_2. Assuming a fixed total ice mass, that is, $M_{tot,1} = M_{tot,2}$, it follows that $N_{p,1}\,m_1 = N_{p,2}\,m_2$. From this, we obtain

$$\gamma = \frac{N_{p,2}}{N_{p,1}} = \frac{m_1}{m_2}. \tag{B1}$$

Given the area-size and mass-size relationships in Section 3.2.2, it holds

$$A_2 = N_{\mathrm{p},2}\, D_2^{\sigma} \tag{B2}$$

$$= N_{\mathrm{p},2} \left(\left(\frac{1}{\gamma} m_1 \right)^{1/\beta} \right)^{\sigma} \tag{B3}$$

$$= \gamma N_{\mathrm{p},1}\, \gamma^{-\sigma/\beta}\, m_1^{\sigma/\beta} \tag{B4}$$

$$= \left(\frac{N_{\mathrm{p},2}}{N_{\mathrm{p},1}} \right)^{1-\sigma/\beta} A_1, \tag{B5}$$

which is equivalent to Equation 10. It follows that $\alpha = 1 - \frac{\sigma}{\beta}$.

Conflict of Interest

The authors declare no conflicts of interest relevant to this study.

Data Availability Statement

The simulation results, along with the plotting script used to reproduce the figures presented in this study, are available in a Zenodo repository (Lottermoser, 2025).

Acknowledgments
This work contributes to the DLR-internal projects H2CONTRAIL and H2EAT. Moreover, both authors received funding from Airbus SAS in the framework of understanding contrails from H_2 propulsion. The authors thank Ziming Wang and Charles Renard for feedback on the initial paper draft. They also thank the reviewers for their valuable comments. This work used resources of the Deutsches Klimarechenzentrum (DKRZ) granted by its Scientific Steering Committee (WLA) under project ID bd0832. Open Access funding enabled and organized by Projekt DEAL.

References

Airbus. (2023). Contrail-chasing blue condor makes airbus' first full hydrogen-powered flight. Retrieved from https://www.airbus.com/en/newsroom/stories/2023-11-contrail-chasing-blue-condor-makes-airbus-first-full-hydrogen-powered

Bier, A., & Burkhardt, U. (2022). Impact of parametrizing microphysical processes in the jet and vortex phase on contrail cirrus properties and radiative forcing. *Journal of Geophysical Research*, *127*(23), e2022JD036677. https://doi.org/10.1029/2022JD036677

Bier, A., Burkhardt, U., & Bock, L. (2017). Synoptic control of contrail cirrus life cycles and their modification due to reduced soot number emissions. *Journal of Geophysical Research*, *122*, 11584–11603. https://doi.org/10.1002/2017JD027011

Bier, A., Unterstrasser, S., Zink, J., Hillenbrand, D., Jurkat-Witschas, T., & Lottermoser, A. (2024). Contrail formation on ambient aerosol particles for aircraft with hydrogen combustion: A box model trajectory study. *Atmospheric Chemistry and Physics*, *24*(4), 2319–2344. https://doi.org/10.5194/acp-24-2319-2024

Bock, L., & Burkhardt, U. (2016). The temporal evolution of a long-lived contrail cirrus cluster: Simulations with a global climate model. *Journal of Geophysical Research*, *121*(7), 3548–3565. https://doi.org/10.1002/2015JD024475

Bräuer, T., Voigt, C., Sauer, D., Kaufmann, S., Hahn, V., Scheibe, M., et al. (2021). Reduced ice number concentrations in contrails from low-aromatic biofuel blends. *Atmospheric Chemistry and Physics*, *21*(22), 16817–16826. https://doi.org/10.5194/acp-21-16817-2021

Burkhardt, U., Bock, L., & Bier, A. (2018). Mitigating the contrail cirrus climate impact by reducing aircraft soot number emissions. *npj Climate and Atmospheric Science*, *1*(1), 37. https://doi.org/10.1038/s41612-018-0046-4

Burkhardt, U., & Kärcher, B. (2011). Global radiative forcing from contrail cirrus. *Nature Climate Change*, *1*(1), 54–58. https://doi.org/10.1038/nclimate1068

Cziczo, D. J., Froyd, K. D., Hoose, C., Jensen, E. J., Diao, M., Zondlo, M. A., et al. (2013). Clarifying the dominant sources and mechanisms of cirrus cloud formation. *Science*, *340*(6138), 1320–1324. https://doi.org/10.1126/science.1234145

Dischl, R., Sauer, D., Voigt, C., Harlaß, T., Sakellariou, F., Märkl, R., et al. (2024). Measurements of particle emissions of an A350-941 burning 100% sustainable aviation fuels in cruise. *Atmospheric Chemistry and Physics*, *24*(19), 11255–11273. https://doi.org/10.5194/acp-24-11255-2024

Forster, L., Emde, C., Unterstrasser, S., & Mayer, B. (2012). Effects of three-dimensional photon transport on the radiative forcing of realistic contrails. *Journal of the Atmospheric Sciences*, *69*(7), 2243–2255. https://doi.org/10.1175/JAS-D-11-0206.1

Gierens, K. (2003). On the transition between heterogeneous and homogeneous freezing. *Atmospheric Chemistry and Physics*, *3*(2), 437–446. https://doi.org/10.5194/acp-3-437-2003

Gierens, K. (2012). Selected topics on the interaction between cirrus clouds and embedded contrails. *Atmospheric Chemistry and Physics*, *12*(24), 11943–11949. https://doi.org/10.5194/acp-12-11943-2012

Hansen, J. E., & Travis, L. D. (1974). Light scattering in planetary atmospheres. *Space Science Reviews*, *16*(4), 527–610. https://doi.org/10.1007/BF00168069

Heymsfield, A. J., Lewis, S., Bansemer, A., Iaquinta, J., Miloshevich, L. M., Kajikawa, M., et al. (2002). A general approach for deriving the properties of cirrus and stratiform ice cloud particles. *Journal of the Atmospheric Sciences*, *59*(2), 3–29. https://doi.org/10.1175/1520-0469(2002)059<0003:agafdt>2.0.co;2

Hofer, S., & Gierens, K. (2025). Synoptic and microphysical lifetime constraints for contrails. *Atmospheric Chemistry and Physics*, *25*(16), 9235–9247. https://doi.org/10.5194/acp-25-9235-2025

Hofer, S., Gierens, K., & Rohs, S. (2024). Contrail formation and persistence conditions for alternative fuels. *Meteorologische Zeitschrift*, *33*(1), 43–49. https://doi.org/10.1127/metz/2024/1178

Irvine, E. A., Hoskins, B. J., & Shine, K. P. (2014). A Lagrangian analysis of ice-supersaturated air over the North Atlantic. *Journal of Geophysical Research*, *119*(1), 90–100. https://doi.org/10.1002/2013JD020251

Iwabuchi, H., Yang, P., Liou, K., & Minnis, P. (2012). Physical and optical properties of persistent contrails: Climatology and interpretation. *Journal of Geophysical Research*, *117*(D6), D06215. https://doi.org/10.1029/2011JD017020

Kärcher, B., Burkhardt, U., Bier, A., Bock, L., & Ford, I. J. (2015). The microphysical pathway to contrail formation. *Journal of Geophysical Research*, *120*(15), 7893–7927. https://doi.org/10.1002/2015JD023491

Kärcher, B., Mayer, B., Gierens, K., Burkhardt, U., Mannstein, H., & Chatterjee, R. (2009). Aerodynamic contrails: Microphysics and optical properties. *Journal of the Atmospheric Sciences*, *66*(2), 227–243. https://doi.org/10.1175/2008JAS2768.1

Kärcher, B., & Yu, F. (2009). Role of aircraft soot emissions in contrail formation. *Geophysical Research Letters*, *36*, L01804. https://doi.org/10.1029/2008GL036649

Kleine, J., Voigt, C., Sauer, D., Schlager, H., Scheibe, M., Jurkat-Witschas, T., et al. (2018). In situ observations of ice particle losses in a young persistent contrail. *Geophysical Research Letters*, *45*(24), 13553–13561. https://doi.org/10.1029/2018GL079390

Koop, T., Luo, B., Tsias, A., & Peter, T. (2000). Water activity as the determinant for homogeneous ice nucleation in aqueous solutions. *Nature*, *406*(6796), 611–614. https://doi.org/10.1038/35020537

Lawson, R., Heymsfield, A., Aulenbach, S., & Jensen, T. (1998). Shapes, sizes and light scattering properties of ice crystals in cirrus and a persistent contrail during SUCCESS. *Geophysical Research Letters*, *25*(9), 1331–1334. https://doi.org/10.1029/98GL00241

Lee, D. S., Fahey, D. W., Skowron, A., Allen, M. R., Burkhardt, U., Chen, Q., et al. (2021). The contribution of global aviation to anthropogenic climate forcing for 2000 to 2018. *Atmospheric Environment*, *244*, 117834. https://doi.org/10.1016/j.atmosenv.2020.117834

Lewellen, D. C. (2012). Analytic solutions for evolving size distributions of spherical crystals or droplets undergoing diffusional growth in different regimes. *Journal of the Atmospheric Sciences*, *69*(2), 417–434. https://doi.org/10.1175/JAS-D-11-029.1

Lewellen, D. C. (2014). Persistent contrails and contrail cirrus. Part 2: Full lifetime behavior. *Journal of the Atmospheric Sciences*, *71*(12), 4420–4438. https://doi.org/10.1175/JAS-D-13-0317.1

Lewellen, D. C., Meza, O., & Huebsch, W. W. (2014). Persistent contrails and contrail cirrus. Part 1: Large-eddy simulations from inception to demise. *Journal of the Atmospheric Sciences*, *71*(12), 4399–4419. https://doi.org/10.1175/JAS-D-13-0316.1

Lottermoser, A. (2025). Plotting script and simulation data of hydrogen contrail-cirrus study [Dataset]. *Zenodo*. https://doi.org/10.5281/zenodo.17094249

Lottermoser, A., & Unterstrasser, S. (2025). High-resolution modeling of early contrail evolution from hydrogen-powered aircraft. *Atmospheric Chemistry and Physics*, *25*(14), 7903–7924. https://doi.org/10.5194/acp-25-7903-2025

Märkl, R. S., Voigt, C., Sauer, D., Dischl, R. K., Kaufmann, S., Harlaß, T., et al. (2024). Powering aircraft with 100% sustainable aviation fuel reduces ice crystals in contrails. *Atmospheric Chemistry and Physics*, *24*(6), 3813–3837. https://doi.org/10.5194/acp-24-3813-2024

McFarquhar, G. M., & Heymsfield, A. J. (1998). The definition and significance of an effective radius for ice clouds. *Journal of the Atmospheric Sciences*, *55*(11), 2039–2052. https://doi.org/10.1175/1520-0469(1998)055⟨2039:TDASOA⟩2.0.CO;2

Mitchell, D. L. (1996). Use of mass- and area-dimensional power laws for determining precipitation particle terminal velocities. *Journal of the Atmospheric Sciences*, *53*(12), 1710–1723. https://doi.org/10.1175/1520-0469(1996)053⟨1710:UOMAAD⟩2.0.CO;2

Mitchell, D. L., Chai, S. K., Liu, Y., Heymsfield, A. J., & Dong, Y. (1996). Modeling cirrus clouds. Part I: Treatment of bimodal size spectra and case study analysis. *Journal of the Atmospheric Sciences*, *53*(20), 2952–2966. https://doi.org/10.1175/1520-0469(1996)053⟨2952:MCCPIT⟩2.0.CO;2

Moore, R. H., Thornhill, K. L., Weinzierl, B., Sauer, D., D'Ascoli, E., Kim, J., et al. (2017). Biofuel blending reduces particle emissions from aircraft engines at cruise conditions. *Nature*, *543*(7645), 411–415. https://doi.org/10.1038/nature21420

Petzold, A., Neis, P., Rütimann, M., Rohs, S., Berkes, F., Smit, H. G. J., et al. (2020). Ice-supersaturated air masses in the northern mid-latitudes from regular in situ observations by passenger aircraft: Vertical distribution, seasonality and tropospheric fingerprint. *Atmospheric Chemistry and Physics*, *20*(13), 8157–8179. https://doi.org/10.5194/acp-20-8157-2020

Ponsonby, J., King, L., Murray, B. J., & Stettler, M. E. J. (2024). Jet aircraft lubrication oil droplets as contrail ice-forming particles. *Atmospheric Chemistry and Physics*, *24*(3), 2045–2058. https://doi.org/10.5194/acp-24-2045-2024

Rubin-Zuzic, M., Bugliaro, L. G., Marsing, A., Voigt, C., Simson, C., Kaiser, S., & Ziegler, P. (2025). Reduced contrail radiative effect for future fleets with low soot and water vapour emissions. *Atmospheric Environment: X*, *27*, 100353. https://doi.org/10.1016/j.aeaoa.2025.100353

Schumann, U. (1996). On conditions for contrail formation from aircraft exhausts. *Meteorologische Zeitschrift*, *5*(1), 4–23. https://doi.org/10.1127/metz/5/1996/4

Schumann, U. (2005). Formation, properties and climatic effects of contrails. *Comptes Rendus Physique*, *6*(4–5), 549–565. https://doi.org/10.1016/j.crhy.2005.05.002

Schumann, U. (2012). A contrail cirrus prediction model. *Geoscientific Model Development*, *5*(3), 543–580. https://doi.org/10.5194/gmd-5-543-2012

Schumann, U., Mayer, B., Gierens, K., Unterstrasser, S., Jessberger, P., Petzold, A., et al. (2011). Effective radius of ice particles in cirrus and contrails. *Journal of the Atmospheric Sciences*, *68*(2), 300–321. https://doi.org/10.1175/2010JAS3562.1

Sölch, I., & Kärcher, B. (2010). A large-eddy model for cirrus clouds with explicit aerosol and ice microphysics and Lagrangian ice particle tracking. *Quarterly Journal of the Royal Meteorological Society*, *136*(653), 2074–2093. https://doi.org/10.1002/qj.689

Soleymani, M., Mostafavi, V., Hebert, M., Kelouwani, S., & Boulon, L. (2024). Hydrogen propulsion systems for aircraft, a review on recent advances and ongoing challenges. *International Journal of Hydrogen Energy*, *91*, 137–171. https://doi.org/10.1016/j.ijhydene.2024.10.131

Teoh, R., Schumann, U., Voigt, C., Schripp, T., Shapiro, M., Engberg, Z., et al. (2022). Targeted use of sustainable aviation fuel to maximize climate benefits. *Environmental Science & Technology*, *56*(23), 17246–17255. https://doi.org/10.1021/acs.est.2c05781

Unterstrasser, S., Gierens, K., Sölch, I., & Wirth, M. (2017). Numerical simulations of homogeneously nucleated natural cirrus and contrail-cirrus. Part 2: Interaction on local scale. *Meteorologische Zeitschrift*, *26*(6), 643–661. https://doi.org/10.1127/metz/2016/0780

Unterstrasser, S. (2014). Large eddy simulation study of contrail microphysics and geometry during the vortex phase and consequences on contrail-to-cirrus transition. *Journal of Geophysical Research*, *119*(12), 7537–7555. https://doi.org/10.1002/2013JD021418

Unterstrasser, S. (2016). Properties of young contrails—A parametrisation based on large-eddy simulations. *Atmospheric Chemistry and Physics*, *16*(4), 2059–2082. https://doi.org/10.5194/acp-16-2059-2016

Unterstrasser, S. (2020). The contrail mitigation potential of aircraft formation flight derived from high-resolution simulations. *Aerospace*, *7*(12), 170. https://doi.org/10.3390/aerospace7120170

Unterstrasser, S., & Gierens, K. (2010a). Numerical simulations of contrail-to-cirrus transition—Part 1: An extensive parametric study. *Atmospheric Chemistry and Physics*, *10*(4), 2017–2036. https://doi.org/10.5194/acp-10-2017-2010

Unterstrasser, S., & Gierens, K. (2010b). Numerical simulations of contrail-to-cirrus transition—Part 2: Impact of initial ice crystal number, radiation, stratification, secondary nucleation and layer depth. *Atmospheric Chemistry and Physics*, *10*(4), 2037–2051. https://doi.org/10.5194/acp-10-2037-2010

Unterstrasser, S., Gierens, K., Sölch, I., & Lainer, M. (2017). Numerical simulations of homogeneously nucleated natural cirrus and contrail-cirrus. Part 1: How different are they? *Meteorologische Zeitschrift*, *26*(6), 621–642. https://doi.org/10.1127/metz/2016/0777

Unterstrasser, S., & Görsch, N. (2014). Aircraft-type dependency of contrail evolution. *Journal of Geophysical Research*, *119*(24), 14015–14027. https://doi.org/10.1002/2014JD022642

Unterstrasser, S., Hoffmann, F., & Lerch, M. (2017). Collection/aggregation algorithms in Lagrangian cloud microphysical models: Rigorous evaluation in box model simulations. *Geoscientific Model Development*, *10*(4), 1521–1548. https://doi.org/10.5194/gmd-10-1521-2017

Unterstrasser, S., & Sölch, I. (2014). Optimisation of simulation particle number in a Lagrangian ice microphysical model. *Geoscientific Model Development*, *7*, 695–709. https://doi.org/10.5194/gmd-7-695-2014

van de Hulst, H. C. (1981). *Light scattering by small particles*. Dover. https://doi.org/10.1002/qj.49708436025

Voigt, C., Kleine, J., Sauer, D., Moore, R. H., Bräuer, T., Le Clercq, P., et al. (2021). Cleaner burning aviation fuels can reduce contrail cloudiness. *Communications Earth & Environment*, *2*(1), 114. https://doi.org/10.1038/s43247-021-00174-y

Voigt, C., Schumann, U., Minikin, A., Abdelmonem, A., Afchine, A., Borrmann, S., et al. (2017). Ml-cirrus: The airborne experiment on natural cirrus and contrail cirrus with the high-altitude long-range research aircraft halo. *Bulletin of the American Meteorological Society*, *98*(2), 271–288. https://doi.org/10.1175/BAMS-D-15-00213.1

Wang, Z., Bugliaro, L., Jurkat-Witschas, T., Heller, R., Burkhardt, U., Ziereis, H., et al. (2023). Observations of microphysical properties and radiative effects of a contrail cirrus outbreak over the North Atlantic. *Atmospheric Chemistry and Physics*, *23*(3), 1941–1961. https://doi.org/10.5194/acp-23-1941-2023

Wölk, J., & Strey, R. (2001). Homogeneous nucleation of H_2O and D_2O in comparison: The isotope effect. *The Journal of Physical Chemistry B*, *105*(47), 11683–11701. https://doi.org/10.1021/jp0115805

Yang, P., Liou, K., Wyser, K., & Mitchell, D. (2000). Parameterization of the scattering and absorption properties of individual ice crystals. *Journal of Geophysical Research*, *105*(D4), 4699–4718. https://doi.org/10.1029/1999JD900755

Yu, F., & Turco, R. P. (1997). The role of ions in the formation and evolution of particles in aircraft plumes. *Geophysical Research Letters*, *24*(15), 1927–1930. https://doi.org/10.1029/97GL01822

Zink, J., Unterstrasser, S., & Jurkat-Witschas, T. (2025). On the potential role of lubrication oil particles in contrail formation for kerosene and hydrogen combustion. *Journal of Geophysical Research*, *130*(12), e2025JD043487. https://doi.org/10.1029/2025jd043487